Chapter 24

Meshless smoothed point interpolation methods for damage modelling

Chapter details

Chapter DOI:

https://doi.org/10.4322/978-65-86503-83-8.c24

Chapter suggested citation / reference style:

Gori, Lapo (2022). "Meshless smoothed point interpolation methods for damage modelling". *In* Jorge, Ariosto B., et al. (Eds.) *Fundamental Concepts and Models for the Direct Problem*, Vol. II, UnB, Brasilia, DF, Brazil, pp. 959–1006. Book series in Discrete Models, Inverse Methods, & Uncertainty Modeling in Structural Integrity.

P.S.: DOI may be included at the end of citation, for completeness.

Book details

Book: Fundamental Concepts and Models for the Direct Problem

Edited by: Jorge, Ariosto B., Anflor, Carla T. M., Gomes, Guilherme F., & Carneiro, Sergio H. S.

Volume II of Book Series in:

Discrete Models, Inverse Methods, & Uncertainty Modeling in Structural Integrity

Published by: UnB City: Brasilia, DF, Brazil Year: 2022

DOI: https://doi.org/10.4322/978-65-86503-83-8

Meshless smoothed point interpolation methods for damage modelling

Lapo Gori[1*]

[1]Department of Structural Engineering, Federal University of Minas Gerais, Brazil.
E-mail: lapo@dees.ufmg.br

[*]Corresponding author

Abstract

Damage models represent an important tool for the analysis of the degradation of quasi-brittle media and, due to their continuous formulation, present certain advantages with respect to other modelling strategies. However, they also exhibit a number of issues when combined with the standard finite element method, like mesh-objectivity and mesh-bias, that can significantly affect the results of a simulation. Due to their nature, meshless techniques are a valid candidate to deal with such issues. The lack of an element-like connectivity between the meshless nodes can allivi-ate the mesh-bias in damage propagation, while the intrinsic nonlocality of meshless approximation functions can act as a regularisation technique at the numerical level. The present work aims to review the application of a specific class of meshless methods, the smoothed point interpolation methods (SPIMs) to the problem of damage modelling.

Keywords: meshless methods; smoothed point interpolation methods; damage mechanics; strain localisation

1 Introduction

In order to solve the system of partial differential equations (PDEs) governing a problem of continuum mechanics (or any other continuum problem representable in terms of PDEs), the finite element method (FEM) *discretises* the problem domain with a *mesh* (see, e.g. Bathe [1996] or Zienkiewicz and Taylor [2000]), in the following manner:

> "
> 1. The continuum is separated by imaginary lines or surfaces into a number of "finite elements".
> 2. The elements are assumed to be interconnected at a discrete number of nodal points situated on their boundaries and occasionally in their interior.
>
> "[Zienkiewicz and Taylor, 2000, pag. 18]

The unknown parameters of the problem are then represented by the nodal values of the field variable (e.g. the displacement field in a solid mechanics problem). The choice of proper approximation functions within each element allows to mount a system of linear equations for the solution of the problem. On the other hand:

> "The meshfree method is used to establish a system of algebraic equations for the whole problem domain without the use of a predefined mesh, or uses easily generable meshes in a much more flexible or "freer" manner. Meshfree methods essentially use a set of nodes scattered within the problem domain as well as on the boundaries to represent the problem domain and its boundaries. The field functions are then approximated locally using these nodes."[Liu, 2009, pag. 14]

As pointed out by Liu in his book [Liu, 2009], the standard finite element method suffers for a number of limitations. Among them there are:

- the need for a quality mesh, that reduces the automation in mesh generation;
- the "overly stiff" behaviour, resulting from the full compatibility in the assumed displacement field, and leading to locking and poor solutions in gradient/derivatives;
- the loss of accuracy due to element distorsions in problems with large deformations;
- the mesh bias in problems like crack growth and phase transformations;
- the difficult simulation of breakage and fragmentation problems;
- the costly adaptive and remeshing approaches;
- the availability of solely a "lower bound" to the exact solution.

An examination of this list reveals that most of the mentioned issues are due to the "heavy and rigid reliance on the use of quality elements that are the building blocks of FEM " [Liu, 2009, pag. 17], and to the predefined connectivity required by such elements.

The basic idea of meshless methods is then to mitigate these issues by eliminating or reducing the reliance on a mesh[1]. Among the most common meshless methods there are the *smoothed particle hydrodynamics* (SPH) method [Gingold and Monaghan, 1977], the *element-free Galerkin*[2] (EFG) method [Belytschko et al., 1994], the *reproducing kernel particle method* (RKPM) [Liu et al., 1995], the family of *point interpolation methods* (which the smoothed point interpolation methods discussed in this manuscript belong to), and the *meshless local Petrov-Galerkin* (MLPG) method [Atluri and Zhu, 1998]. Despite a computational cost that is, in general, higher than in the standard FEM, meshless methods exhibit a number of important features. Among them, the following can be highlighted [Liu, 2009]:

- easy automatic mesh generation using triangulation strategies;
- absent or limited mesh alignment sensitivity;
- no need for remeshing operations, especially in problems with large deformations or moving discontinuities;

---

[1] Though meshless discretisations are not based on a conventional mesh as intended in the standard FEM, the term "mesh" will still be used in the following to indicate such discretisations.

[2] Based on the *diffuse elements method* (DEM) originated by Nayroles et al. [1992].

- construction of shape functions of any desired order of continuity.

Regarding physically nonlinear problems, and especially the problem of *continuum damage mechanics* discussed in this manuscript, the standard FEM suffers for other issues besides the aformentioned ones. The presence of damage indeed, results in a *strain-softening* behaviour. Numerical simulations of strain-softening problems, where *localisation* occours, performed with the standard finite element method (FEM), are usually affected by certain pathological behaviours, such as *strong mesh-dependency*, *premature fracture initiation*, and *instantaneous perfectly-brittle fracture* [de Borst et al., 1993, Peerlings et al., 2002]. These pathological effects are due to the fact that, at a certain load level, the continuum boundary value problem may become *ill-posed* (the so-called loss of ellipticity of the equilibrium equations), resulting in an infinite set of solutions (discontinuous bifurcation), from which the numerical method selects the one corresponding to the smallest energy dissipation. This approximated solution strongly depends on the mesh; at mesh refinement it tends to a failure with zero energy dissipation, and then to a *nonphysical* behaviour.

It has been pointed out that the pathological behaviours that may affect the numerical simulations where localisation occours are due to the *local* representation offered by the classic continuum theory, in contrast with the *nonlocal* nature of phenomena like damage and plasticity [Bažant, 1991]. The main aim of the proposed solutions to this problem (the so-called regularisation techniques) is the introduction of an *internal length* in the continuum model, allowing to recover the nonlocal character of the phenomenon; an interesting overview on the different regularisation methods can be found in the papers by de Borst et al. [de Borst et al., 1993] and by Bažant et al. [Bažant and Jirásek, 2002].

Some classes of meshless methods have been shown to be capable to deal with the aformentioned localisation issues, due to their intrinsic nonlocal character. As pointed out in a paper by Chen et al. [Chen et al., 2000], the nonlocality of these methods is due to the fact that their approximation functions are not constructed locally as in the finite element method, because of the use of basis and weighting functions with support size greater than the nodal spacing. In the same paper the authors pointed out the analogy between MLS/RK approximations and gradient-enhanced models, and also showed the beneficial effects on localisation associated to the use of an assumed strain method where the nonlocal equivalent strain measure is directly approximated in terms of displacement parameters. Moreover, the use of a meshless method allows, in general, to overcome the problem of mesh orientation bias, that may appear in damage propagation problems. Among the methods that have been shown to possess certain regularisation effects in localisation problems there are *moving least square* (MLS) and *reproducing kernel* (RK) approximations, as well as methods based on *strain smoothing* techniques [Liu et al., 1999, Chen et al., 2000, Li et al., 2000, Chen et al., 2004, 2007, Wang and Li, 2012, Pozo et al., 2014]. As strain smoothing methods, also the *smoothed point interpolation methods* (SPIMs) discussed in this manuscript have been shown to exhibit regularisation properties, as illustrated by Gori et al. [Gori et al., 2019b], both alone as well as when combined with other regularisation strategies, like the micropolar continuum theory [Gori et al., 2019a,c]. Particle methods, like the SPH, have also been shown to be capable to deal with strain-softening problems [Vignjevic et al., 2014].

One of the main issues in the most common meshfree approaches is the lack of the Kronecker delta property, which requires a special treatment for the imposition of essential boundary conditions, like the use of the well-known *Lagrange multipliers* and *penalty* methods or other procedures [Chen and Wang, 2000, Wu and Plesha, 2002, Fernández-Méndez and Huerta, 2004]. The smoothed point interpolation methods discussed in this manuscript [Liu, 2009, 2010a,b, Liu and Zhang, 2013] allow for a more simple imposition of boundary conditions, since they are based on shape functions constructed with the *point interpolation method* (PIM), which guarantee the Kronecker delta property. The price for a more simple imposition of the boundary conditions is the presence of *incompatible* shape function, which may present discontinuities in the problem domain, requiring the use of a so-called *weakened-weak* form of the continuum problem [Liu, 2010a,b] based on a *strain smoothing technique* [Liu, 2008]. Regarding the field of continuum mechanics, these methods have been applied to linear elasticity [Liu, 2010b] and elasto-plasticity [Zhang et al., 2015]. The smoothing operation which these methods are based on is a sort of generalisation of the *Stabilised Conforming Nodal Integration* (SCNI) technique originally proposed by Chen et al. [Chen et al., 2001].

1.1 Outline

The outline of this manuscript is organised as follows. In the first section after this introduction (Section 2), the fundamental aspects of meshless methods, like discretisation, field variables approximation, and numerical integration, are reviewed, and compared with the approach of the standard FEM. Section 3 is the core of the manuscript; it discusses in details the main aspects of smoothed point interpolation methods, and their application to problems of continuum damage mechanics (more specifically, to problems with scalar damage). Section 4 briefly discusses the issue of localisation in strain-softening problems, and the different regularisation strategies that can be applied to scalar damage problems and to other problems where localisation may occour. Finally, Section 5 illustrates some numerical results obtained with SPIM stategies applied to damage problems, while Section 6 presents some concluding remarks.

1.2 Notations and tools

Some standard notations used in the body of the manuscript are summarised here. The symbol $\mathbf{D} \subset \mathbf{E}$ indicates the domain of a body embedded in the three-dimensional Euclidean space $\mathbf{E}$, and $\mathbf{D}_k^S \subset \mathbf{D}$ one of its subsets, referred to as *smoothing domain*. *Vectors* are indicated as $\bar{\boldsymbol{x}} \in \bar{\mathbf{E}}$, with $\bar{\boldsymbol{x}} = x_i \, \bar{\boldsymbol{e}}_i$, where $\bar{\boldsymbol{E}}$ is the vector space associated to $\mathbf{E}$, and $(\bar{\boldsymbol{e}}_i)$ a basis in $\mathbf{E}$. *Second-order* and *fourth-order* tensors are indicated, respectively, by $\underline{\boldsymbol{x}} \in \bar{\mathbf{E}} \otimes \bar{\mathbf{E}}$, with $\underline{\boldsymbol{x}} = x_{ij} \, \bar{\boldsymbol{e}}_i \otimes \bar{\boldsymbol{e}}_j$, and by $\hat{\mathrm{x}} \in \bar{\mathbf{E}} \otimes \bar{\mathbf{E}} \otimes \bar{\mathbf{E}} \otimes \bar{\mathbf{E}}$, with $\hat{\mathrm{x}} = x_{ijk\ell} \, \bar{\boldsymbol{e}}_i \otimes \bar{\boldsymbol{e}}_j \otimes \bar{\boldsymbol{e}}_k \otimes \bar{\boldsymbol{e}}_\ell$. The symbol "$\cdot$" denotes the standard dot product between vectors and the one index contraction between tensors (or between a tensor and a vector) like, for example, $\bar{\boldsymbol{x}} \cdot \bar{\boldsymbol{y}} = x_i \, y_i$ and $\underline{\boldsymbol{x}} \cdot \bar{\boldsymbol{y}} = x_{ij} \, y_j \, \bar{\boldsymbol{e}}_i$, while the symbol ":" denotes the double contraction between tensors like, for example, $\hat{\mathrm{x}} \cdot \underline{\boldsymbol{y}} = x_{ijk\ell} \, y_{k\ell} \, \bar{\boldsymbol{e}}_i \otimes \bar{\boldsymbol{e}}_j$ and the other possible combinations. With the symbol "$\otimes$", the standard tensor product, as $\bar{\boldsymbol{x}} \otimes \bar{\boldsymbol{y}} = x_i \, y_j \, \bar{\boldsymbol{e}}_i \otimes \bar{\boldsymbol{e}}_j$ or $\underline{\boldsymbol{x}} \otimes \underline{\boldsymbol{y}} = x_{ij} \, y_{k\ell} \, \bar{\boldsymbol{e}}_i \otimes \bar{\boldsymbol{e}}_j \otimes \bar{\boldsymbol{e}}_k \otimes \bar{\boldsymbol{e}}_\ell$, is indicated. In some applications the Voigt notation will be used to represent second-order and fourth-order tensors; once a certain coordinates system has been fixed, a generic second-order tensor with dimension three $\underline{\boldsymbol{x}}$ can be represented by means of an *array* with nine components, indicated with the symbol $\{\underline{\boldsymbol{x}}\}$. In an analogous way, a fourth-order tensor with dimension three $\hat{\mathrm{x}}$ can be represented by means of a 9×9 matrix, indicated as $[\hat{\mathrm{x}}]$. It should be noted that the provided dimensions refer to a general three-dimensional case; in different situations (e.g. plane-strain or plane-stress states, or peculiar symmetries), the size of arrays and matrices in Voigt representation is minor, in general. The same symbols $\{\cdot\}$ and $[\cdot]$ are also used to indicate, respectively, arrays and matrices in numerical equations. The numerical implementations of the strategies discussed in this paper, as well as the numerical simulations, have been performed in the open-source program **INSANE**[3]. The triangular background cells used for the construction of the meshfree discretisations, as well as the contour plots of the results obtained with the meshfree models, have been generated with the program **Gmsh** [Geuzaine and Remacle, 2009].

---

[3] More information on the project can be found at `https://www.insane.dees.ufmg.br/`

2 Fundamentals of meshless methods

Before presenting the fundamentals of meshless methods it's worth it to briefly illustrate the main aspects of the finite element method (FEM); these will be used later to introduce the meshless approach, serving as a basis for the reader that is familiar with the FEM. Given a domain $\mathbf{D}$, an FEM model is contructed as a tesselation of this domain using a finite number of *elements* $\mathbf{D}_e$ that don't overlap and don't leave gaps in the domain (Figure 1); this tesselation is commonly referred to as *mesh*. Finite elements may present different geometrical shapes, depending on the size of the domain of the problem; straight lines and curves in one-dimensional domains, polygons in two-dimensional domains, and polyhedra in three-dimensional domains. Regardless of the peculiar shape of an element, each one of its vertices is a so-called *node* (Figure 1).

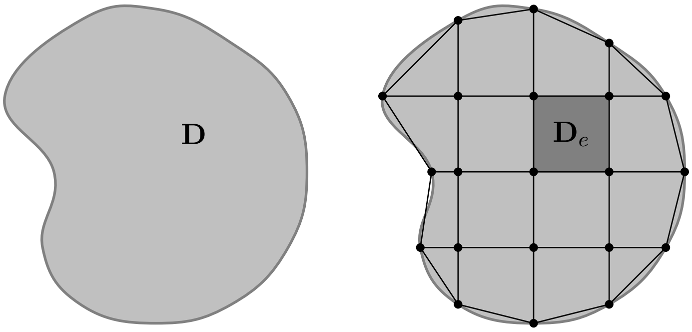

Figure 1: Two-dimensional FEM mesh

The role of the nodes is to discretise the field variables of the problem. A generic continuous problem characterised by the field variable $u(p)$, with p being a point in the domain $\mathbf{D}$, is transformed into a discrete one, where the field variable is only sampled at a finite number of points p_i in the domain, corresponding to the nodes, $u_i = u(p_i)$. Regarding the discretisation of a problem, the elements have a double task. Firstly, they serve as units for the interpolation of the field variables. Once the field variables are known at the nodes of a model, their values can be interpolated inside each element using the so-called shape functions $\mathcal{N}_i$ of the element (Figure 2):

$$u(p) \simeq u^h(p) = \sum_{i=1}^{N} \mathcal{N}_i(p)\, u_i, \qquad p \in \mathbf{D}_e \tag{1}$$

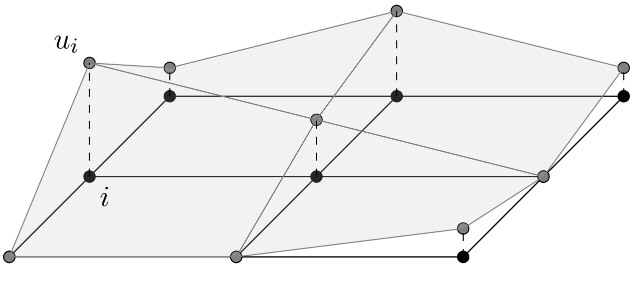

Figure 2: Two-dimensional FEM interpolation

The second task of the elements is to allow the numerical integration of the weak form that describes the behaviour of the problem at hand. Regardless of the kind of problem, a weak form usually requires to perform an integration over the problem domain. In this sense, the tesselation of the domain allows to build a quadrature rule, where the integral is performed considering a certain number of integration points within each element (Figure 3); such points are also referred to as *Gauss points*, since the Gauss quadrature rule is the one usually adopted in the FEM.

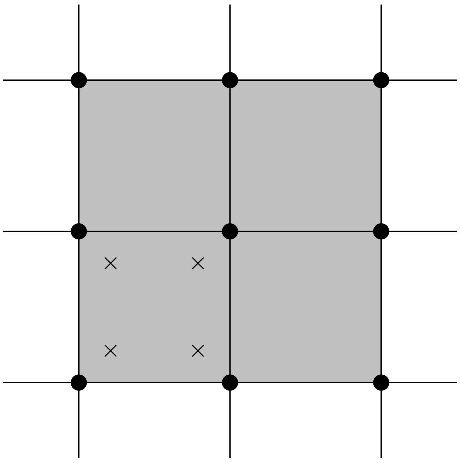

Figure 3: Two-dimensional FEM integration points

Meshless methods still need to perform the aformentioned tasks, i.e. the field variables interpolation and the numerical integration of the weak form. However, while in the FEM these tasks are performed using a single object, the finite element, in meshless methods there are usually two distinct objects, the *support domain*, that allows to perform the interpolation (or approximation), and the *integration domain*, that allows to perform the numerical integration.

2.1 Field variables interpolation/approximation

As pointed out in Section 2, in the FEM the field variables interpolation is element-based, i.e. it's defined within each finite element. In meshless methods on the other hand, the interpolation (or approximation, as it will be pointed out later) is *node-based*, i.e. it only uses the nodes scattered on the domain, without any information about their connectivity. Many meshless methods still use some sort of mesh-like grid for different purposes, but this grid is not stricly needed for the interpolation of the field variables.

As mentioned before, the object responsible for the interpolation is the *support domain*. A support domain S_d (Figure 4) is defined at each interest point $p \in \mathbf{D}$ where the field variables must be interpolated, and is composed by the set of nodes (the so-called *support nodes*) in the neighbourhood of the point p.

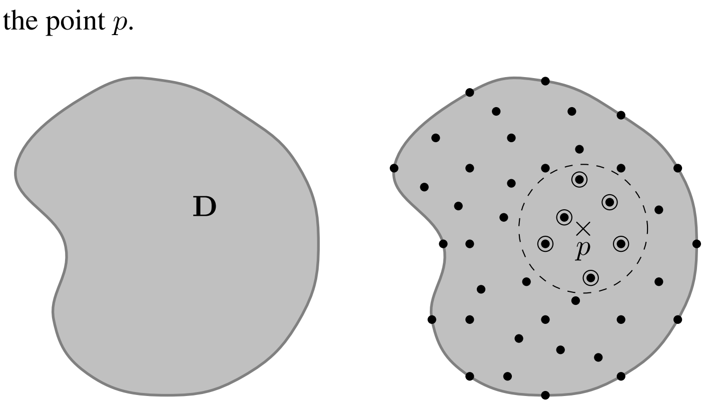

Figure 4: Meshless support domain

Given a point $p \in \mathbf{D}$, the interpolation of a generic field variable $u(p)$ is built using the nodes belonging to the support domain at p:

$$u(p) \simeq u^h(p) = \sum_{i \in S_d(p)} \phi_i(p)\, u_i \tag{2}$$

In the summation above, the terms $u_i = u(p_i)$ are the values of the field variable at the support nodes, and the functions ϕ_i are the shape functions. Unlike FEM shape functions, there isn't always a closed form expression for meshless shape functions; the shape functions for a certain support domain are usually evaluated with a numerical procedure that involves a matrix inversion, resulting in a higher computational cost.

While the concept of support domain is the same for the different meshless method, each method is characterised by it's own strategy for the construction of shape functions[4]. Among the different strategies there are[5]:

- the moving least square (MLS) method;
- the point interpolation method (PIM);
- the radial point interpolation method (RPIM);
- the radial point interpolation method with polynomial reproduction (RPIMp).

In the present section the terms interpolation and approximation have been mentioned; while many meshless shape functions possess the delta Kronecker property, resulting in an interpolation of the field variables, many other shape functions, like the ones obtained with the MLS, don't possess such a property and are only capable to provide an approximation of the field variables.

2.2 Numerical integration

Just like the FEM many meshless methods are based on the weak form of a certain problem (or a weakened-weak form, like for the SPIM strategy discussed in Section 3), that requires a numerical integration over the problem domain. While in the FEM the integration is performed using a quadrature rule within each element, meshless methods perform this operation making use of the so-called *integration domains*. Together with the kind of shape function, the specific type of integration process is a characteristic of each meshless method.

In the present section, the concept of numerical integration for meshless methods is illustrated using the procedure adopted in the EFG method [Belytschko et al., 1994], also similar to the one adopted in the MLPG method [Atluri and Zhu, 1998] and in the PIM [Liu and Gu, 2001]. In these methods the numerical integration is performed in a way that is similar to the FEM integration. As illustrated in Figure 5, the domain is tesselated into integration domains, that may form a regular or an irregular grid. Each integration domain is endowed with integration points, where the approximation functions are evaluated. The main difference with the FEM integration is that in the FEM all the integration points of the same element are supported by the same nodes (i.e. the nodes of the element), while in a meshless method each integration point usually has its own support domain, that may vary from point to point even in the same integration domain (Figure 5).

As it will be shown in Section 3, SPIM strategies are based on a different approach to the numerical integration process, due to the presence of a smoothing operation; the resulting integration

---

[4] Shape functions construction will be discussed with more details in Section 3.1, for the case of smoothed point interpolation methods.

[5] A comprehensive account on the different strategies for the construction of the most common meshless shape functions can be found in Liu [2009]

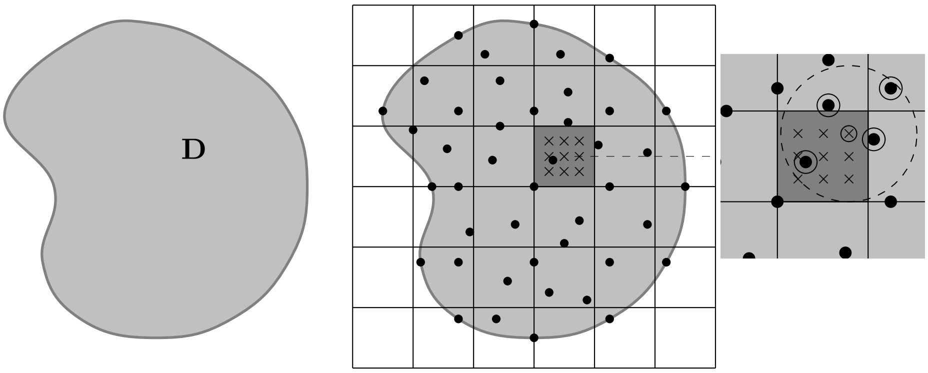

Figure 5: Meshless grid-like integration domains

is similar to the one of the stabilised conforming nodal integration (SNCI) proposed for the EFG method by Chen et al. [2001].

3 Meshless Smoothed Point Interpolation Methods (SPIMs)

Smoothed point interpolation methods, like other meshfree methods, rely on a set of nodes scattered in the problem domain, usually obtained through a triangulation operation. In a smoothed point interpolation method the field variable of the boundary value problem in linear elasticity, i.e. the displacement field $\bar{\boldsymbol{u}}(p)$ at each point $p \in \mathbf{D}$, is approximated as [Liu, 2009]

$$\bar{\boldsymbol{u}}(p) \simeq \sum_{i \in S_d} [\phi_i(p)]\{d_i\} \tag{3}$$

where the index i indicates a node p_i in the *support domain* S_d, i.e. the set of nodes in the neighbourhood of the point $p \in \mathbf{D}$ usually selected using a *T-scheme* [Liu, 2009], $[\phi_i(p)]$ is the nodal matrix of approximation functions, and $\{d_i\}$ is an array containing the nodal parameters of the field variable, i.e. its values $\bar{\boldsymbol{u}}(p_i)$ at each node p_i.

The shape functions, in this class of methods, are usually generated using the *point interpolation method* [Liu and Gu, 2001] (PIM), or the *radial point interpolation method* with or without polynomial reproduction [Wang and Liu, 2002b] (RPIM and RPIMp), and are characterised by the following properties: they are linearly independent, posses the Kronecker delta property, form a partition of unity, posses the linear reproducing property, present compact support, and are *not compatible*. The first meshfree methods based on these shape functions were proposed by Liu and his co-authors in Liu and Gu [2001] and Wang and Liu [2002b], as an alternative to existent meshfree methods. Indeed, due to their *delta Kronecker* property they allowed a more simple imposition of essential boundary conditions, with respect to other meshfree methods.

As pointed out above, however, the price for the delta Kronecker property is a lack of compatibility of the shape functions, meaning that the approximated fields may exhibit *discontinuities* when passing from a support domain to another. This makes such shape functions unable to satisfy the requirement of *square integrable first derivatives* needed for the formulation of standard weak forms. In order to overcome this issu, Liu [Liu, 2010a,b] proposed the use of a *weakened-weak form* of the elastic problem, based on a *smoothing operation*[6] [Liu, 2008] applied to the gradi-

---

[6] As mentioned by Liu (see, e.g. the introduction of Liu [2010a]) such smoothing technique [Liu, 2008] is analogous to the one adopted in other contextes like non-local continuum mechanics [Zhang et al., 2006, Eringen and Edelen, 1972], SPH methods [Liu and Liu, 2003, Lucy, 1977, Liu et al., 2008, Monaghan, 1982], hybrid FEM [Quarteroni and Valli, 1994], for the regularisation of spatial instabilities in nodal

ents involved in the formulation, that allows to reduce the continuity requirement of the shape functions.

The combination of the smoothing technique with point interpolation functions allowed to obtain different smoothed meshfree methods[7][8], like the *node-based smoothed point interpolation* (NS-PIM) method [Liu et al., 2005, Zhang et al., 2007], the *edge-based smoothed point interpolation* (ES-PIM) method [Liu and Zhang, 2008], and the *cell-based smoothed point interpolation method* [Liu and Zhang, 2009]. In order to deal with the presence of incompatible shape functions and smoothing operations, Liu developed a new theoretical framework, establishing two novel concepts: the *G-space theory* and the *weakened-weak form* (W^2) formulation (see, e.g. Liu [2010a,b], Liu and Zhang [2013]). These concepts were later extended to the case of the micropolar continuum theory by Gori et al. [2019c].

3.1 Shape functions

As pointed out above, three types of shape functions are commonly used in SPIMs strategies: PIM, RPIM and RPIMp. The present section focuses on shape functions obtained with the radial point interpolation method with polynomial reproduction, since they are the ones adopted in the numerical simulations of Section 5. Furthermore, the formulation of RPIMp shape function is more general and PIM and RPIM shape functions can be obtained as special cases.

The RPIMp approximation of a function u is expressed by

$$u(q) \simeq u^h(q) = \sum_{i=1}^{n} R_i(q) a_i + \sum_{j=1}^{m} p_j(q) b_j = \{R(q)\}^T \{a\} + \{p(q)\}^T \{b\} \tag{4}$$

where the terms $R_i(q)$ are a set of radial functions evaluated at q, constituting a radial basis, n is the number of support nodes in the local support domain at the point q, the terms $p_j(q)$ constitute a polynomial basis, and m is the number of monomials composing the polynomial basis. The number of monomials should be sufficient to guarantee, at least, the linear reproduction (e.g. in a two-dimensional domain three monomials are sufficient to pass the standard patch test, the constant term and the two linear terms in the coordinates x and y). The approximation of Equation 4 is characterised by two sets of unknown coefficients:

$$\{a\} = \left(a_1, \ldots, a_n\right)^T, \quad \{b\} = \left(b_1, \ldots, b_m\right)^T \tag{5}$$

which can be evaluated imposing the interpolation condition

$$u_k = \sum_{i=1}^{n} R_i(q_k) a_i + \sum_{j=1}^{m} p_j(q_k) b_j, \quad k = 1, \ldots, n \tag{6}$$

and the following additional condition [Golberg et al., 1999]:

$$\sum_{i=1}^{n} p_j(q_i) a_i = 0, \quad j = 1, \ldots, m \tag{7}$$

---

integrated meshfree methods Chen et al. [2001], and for the regularisation of material instabilities [Chen et al., 2000].

[7] The smoothing technique has been also applied by Liu and his co-authors to the standard FEM, obtaining the so-called *smoothed finite element method* (see, e.g. Liu et al. [2007] and Liu et al. [2009]).

[8] As pointed out in Liu and Zhang [2013], the smoothed point interpolation methods belong to the more general class of *strain constructed* methods, which still relies on point interpolation function, but with a different strategy for the treatement of the gradients.

that can be recast in the following compact form:

$$\left\{\begin{array}{lcl}\{U\} & = & [R_q]\{a\}+[P_m]\{b\} \\ \{0\} & = & [P_m]^T\{a\}\end{array}\right. \rightarrow \begin{pmatrix}[R_q] & [P_m] \\ [P_m]^T & [0]\end{pmatrix}\begin{pmatrix}\{a\} \\ \{b\}\end{pmatrix}=\begin{pmatrix}\{U\} \\ \{0\}\end{pmatrix} \tag{8}$$

where the matrix $[R_q]$ with dimension $n \times n$ is the *moment matrix*, each line of which is composed by the radial basis function evaluated at a support node, while the matrix $[P_m]$ with dimension $n \times m$ has its lines formed by the polynomial basis evaluated at the support nodes:

$$[R_q]=\begin{pmatrix}\{R(q_1)\}^T \\ \vdots \\ \{R(q_n)\}^T\end{pmatrix}, \quad [P_m]=\begin{pmatrix}\{p(q_1)\}^T \\ \vdots \\ \{p(q_n)\}^T\end{pmatrix} \tag{9}$$

After some manipulations of the involved equations (see, e.g. Liu [2009]), the unknown coefficients can be evaluated as

$$\{a\}=[S_a]\{U\}, \quad \{b\}=[S_b]\{U\} \tag{10}$$

where the matrices $[S_a]$ and $[S_b]$ are represented by

$$[S_a]:=[R_q]^{-1}-[R_q]^{-1}[P_m][S_b] \tag{11}$$

$$[S_b]:=\left([P_m]^T[R_q]^{-1}[P_m]\right)^{-1}[P_m]^T[R_q]^{-1} \tag{12}$$

resulting in the approximation

$$u^h(q)=\left(\{R(q)\}^T[S_a]+\{p(q)\}^T[S_b]\right)\{U\}=\{\phi(q)\}^T\{U\} \tag{13}$$

where each *shape function* $\phi_i(q)$ is given by

$$\phi_i(q)=R_j(q)[S_a]_{ji}+p_j(q)[S_b]_{ji} \tag{14}$$

The *radial functions* $R_i(p)$ appearing in Equation 4 defined for each node i in the support domain, depend only on the distance r_i between the point $p \in \mathbf{D}$ at which they must be evaluated and the node i. In the numerical simulations presented in Section 5 the following *exponential* (EXP) function was adopted:

$$R_i(r_i)=\exp\left(-cr_i^2\right) \tag{15}$$

depending on the shape parameter c [Wang and Liu, 2002b]. Investigations on the choice of optimal shape parameters for the accuracy of the approximation can be found in Wang and Liu [2002b] and Wang and Liu [2002a], for example. However, as pointed out in Liu [2009], in presence of polynomial terms as in the RPIMp, and when smoothing techniques are adopted, the reliance of the accuracy on the shape parameters is significantly reduced.

By neglecting the polynomial term $\{p(q)\}^T\{b\}$ appearing in Equation 4 it's possible to obtain the formulation of of RPIM shape functions. PIM shape functions, on the other hand, can be obtained by neglecting the same term $\{p(q)\}^T\{b\}$ and by replacing the radial functions R_i with polynomial functions.

3.1.1 Shape functions properties

As already pointed out, the main advantage of PIM, RPIM and RPIMp shape functions over other common meshless shape functions is the delta Kronecker property, that allows a more simple imposition of boundary conditions. This property is obtained at the price of possible discontinuities of the shape functions over the domain, resulting in incompatible shape functions. According to

Liu [2009], these discontinuities are due to the absence of a *smooth transition* between support domains. When passing from an integration point to another, with different support domains, the shape function for a node changes suddenly, resulting in a discontinuity at that point. This doesn't happen, for example, in the *moving least square* (MLS) method [Liu, 2009], where the presence of weight functions allows for a smooth transition between support domains; MLS shape functions indeed, are compatible, in general.

PIM, RPIM and RPIMp shape functions require a matrix inversion operation in order to be evaluated at each interest point, and may suffer from singularity issues. PIM functions are more prone to the singularity of the moment matrix, that may occour due to peculiar alignments of the support nodes [Liu, 2009]. The moment matrix of RPIM and RPIMp, in general, is not singular and, as pointed out by Liu [2009], the construction of an RPIMp approximation is possible as long as the matrix $[P_m]^T[R_q]^{-1}[P_m]$ appearing in Equation 12 is invertible; the invertibility of such matrix is guaranteed, in general, as long as $n \geq m$.

Despite being more complex, RPIMp shape functions are usually preferred over the two other strategies, because of the singularity issues of PIM interpolations and because RPIM functions lack of consistency, in the sense that they don't exhibit polynomial reproduction of any order, meaning that they cannot pass the standard *patch test*.

3.1.2 Support nodes selection strategies

In order to construct a meshless approximation at a certain point q of the problem domain it is necessary to use a number of n *support nodes*, composing the so-called *support domain* at the point q. In order to compose the support domain by selecting proper nodes in the neighbourhood of the point q, two different strategies have been adopted in this work: the selection via *influence domains* and via *T-schemes*[9].

The selection of support nodes via *influence domains* is a standard approach adopted in a number of meshfree methods. Each node is endowed with an *influence domain*, characterised by a *shape* and its *dimensions*. For example, in Figure 6, each node possesses a *circular* influence domain, characterised by a certain radius which may vary from node to node. For each integration point, the corresponding support domain is generated adding all the nodes which influence domains contain the selected integration point. In the example depicted in Figure 6, the support domain at the selected integration have been marked with an hollow circle. The number of nodes in each support domain is controlled by the ratio between the size of the influence domains and the mean nodal distance. While this method works well for MLS and RPIM shape functions, when applied to PIM shape functions it may lead to a singular moment matrix, in case of peculiar nodal alignments.

An alternative is represented by the so-called *T-schemes* [Liu, 2009]. Such methods perform the support nodes selection making use of *background triangular cells*, constructed as a triangulation of the scattered nodes of the discrete model. In general, there is no need to construct such set of cells specifically for the application of the T-schemes. A triangulation indeed, could have been already constructed during the discretisation of the domain, at the moment of the nodes generation. Furthermore, in smoothed point interpolation methods, like the ones considered in

---

[9] Another strategy, that hasn't been considered in this treatise but that could improve the performances of this class of meshfree methods, especially in case of large models, is the support nodes selection via *K-Nearest Neighbor* (KNN) algorithms, that could also be useful as an alternative to the methods considered in this treatise for the investigation of the regularisation properties related to the non-locality of PIM and RPIM approximations. As pointed out in 3.1.3, the use of the influence domains strategy tends to affect the sparseness of the stiffness matrix in a negative way; in this case, KNN strategies should introduce a non-locality analogous to the one of the influence domains strategy, with a reduced effect on the sparseness of the stiffness matrix.

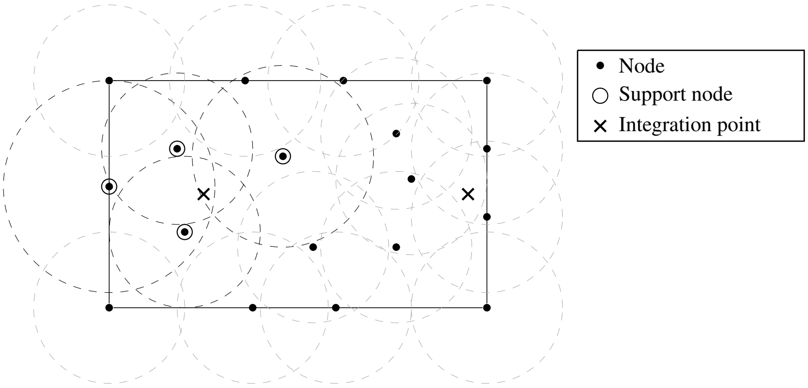

Figure 6: Support nodes selection via influence domains

this treatise, a set of background cells is necessary for the construction of the *smoothing domains* (Section 3.2); hence, the triangular cells are already available for nodes selection. In the examples presented in Section 5, two kind of T-schemes have been considered: the *T3-scheme* and the *T6/3-scheme*, which, as pointed out by Liu [Liu, 2009], allow to obtain invertible moment matrices with both PIM and RPIM shape functions[10]. For an integration point belonging to a certain cell, the T3-scheme selects as support nodes the three nodes at the vertices of the cell (Figure 7(a)). The T6/3-scheme distinguishes between *interior* and *boundary* cells. The former are cells which have no one of their edges on the boundary of the problem domain, while the latter are cells with at least an edge on the boundary of the domain. For a boundary cell, the three nodes at the vertices of the cell are selected as support nodes, like in the T3-scheme. On the other hand, in case of an interior cell, a total number of six nodes is selected: the three nodes located at the vertices of the cell, and three nodes located at the remote vertices of the three neighbouring cells (Figure 7(b)).

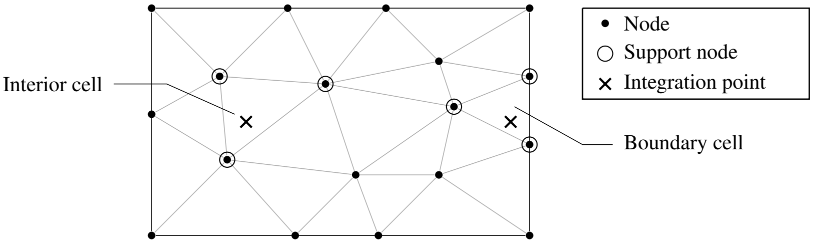

(a) T3-scheme

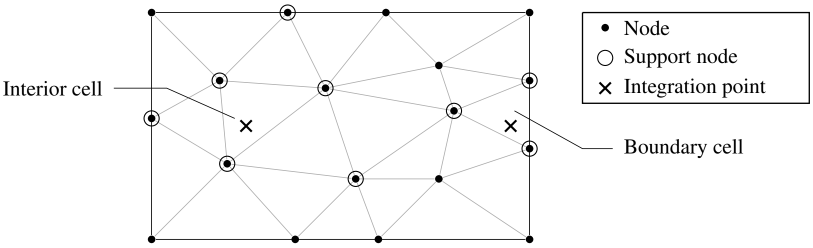

(b) T6/3-scheme

Figure 7: Support nodes selection via T-schemes

---

[10] As pointed out in Liu [2009], two further methods based on triangular background cells are available, the so-called T6 and T2L schemes, which selects, in general, a larger number of nodes with respect to the T-schemes already mentioned in this section. However, the example discussed in Section 5 focused only on the two T-schemes discussed in this section.

3.1.3 T-schemes vs influence domains

It has been mentioned that T-schemes are useful to guarantee the invertibility of the moment matrix in the PIM strategy. As pointed out by Liu [2009], they are also important to obtain a *sparse* stiffness matrix, which eases the solution of the linear system of equations. The sparseness of the stiffness matrix results from the *compact* character of the support domains generated with the T-schemes. Another interesting feature is that they also allow to know *a priori* the parts of the domain where the approximation functions may exhibit discontinuities, which is important for the node- and edge-based methods presented in Section 3.2.2. The influence domains strategy on the contrary, depending on the size of the influence domains, tends to destroy the sparseness of the stiffness matrix. Furthermore, when using the influence domains strategy, the positions of the shape functions discontinuities is not known *a priori.* Despite these disadvantages, this strategy was adopted in the simulations of Section 5.1 in order to investigate the non-local effects of the PIM and RPIM meshfree methods.

3.2 Smoothing domains creation and weakened-weak form

As pointed out in the beginning of Section 3, the use of *incompatible* approximation functions led Liu and his co-authors to the introduction of a novel theoretical structure, constituted by the *G-space theory* and the *weakened-weak form* (W^2) formulation (see, e.g. Liu [2010a,b] and Liu and Zhang [2013]), which will be briefly recalled here. First, the concept of weak form in classic elasticity is briefly recalled. Then, the novel formulation introduced by Liu and his co-authors is recalled, focusing on the following points:

- smoothing domains generation;
- smoothing operation;
- G-spaces;
- weakened-weak form.

3.2.1 Weak form in classic elasticity

For a problem of classic elasticity, characterised by the unknown field variable $\bar{\boldsymbol{u}}$ defined over the problem domain $\mathbf{D}$, by the essential boundary condition $\bar{\boldsymbol{u}} = \bar{\boldsymbol{u}}^*$ at $\partial\mathbf{D}_e$, by the natural boundary condition $\bar{\boldsymbol{n}} \cdot \underline{\boldsymbol{\sigma}} = \bar{\boldsymbol{t}}$ at $\partial\mathbf{D}_n$, and subjected to volume forces $\bar{\boldsymbol{b}}_V$ defined over the whole domain $\mathbf{D}$, the weak form of the problem can be expressed as in the following: find the field $\bar{\boldsymbol{u}} \in \mathcal{V}(\mathbf{D})$ such that

$$\int_{\mathbf{D}} \underline{\boldsymbol{\varepsilon}}(\bar{\boldsymbol{w}}) : \left(\hat{\mathbf{E}} : \underline{\boldsymbol{\varepsilon}}(\bar{\boldsymbol{u}})\right) \,\mathrm{d}\mathcal{V} - \int_{\partial\mathbf{D}_n} \bar{\boldsymbol{w}} \cdot \bar{\boldsymbol{t}} \,\mathrm{d}\mathcal{S} - \int_{\mathbf{D}} \bar{\boldsymbol{w}} \cdot \bar{\boldsymbol{b}}_V \,\mathrm{d}\mathcal{V} = 0, \quad \forall \bar{\boldsymbol{w}} \in \mathcal{V}^0(\mathbf{D}) \tag{16}$$

where $\underline{\boldsymbol{\varepsilon}}(\bar{\boldsymbol{u}}) = (u_{i,j} + u_{j,i})/2 \; \bar{\boldsymbol{e}}_i \otimes \bar{\boldsymbol{e}}_j$, and where $\mathcal{V}(\mathbf{D})$ and $\mathcal{V}^0(\mathbf{D})$ are, respectively, the spaces of *trial* and *test* functions, defined as

$$\mathcal{V}(\mathbf{D}) := \left\{\bar{\boldsymbol{u}} \in \left(\mathcal{H}^1(\mathbf{D})\right)^n \mid \bar{\boldsymbol{u}} = \bar{\boldsymbol{u}}^* \text{ at } \partial\mathbf{D}_e^u\right\} \tag{17}$$

$$\mathcal{V}^0(\mathbf{D}) := \left\{\bar{\boldsymbol{w}} \in \left(\mathcal{H}^1(\mathbf{D})\right)^n \mid \bar{\boldsymbol{w}} = 0 \text{ at } \partial\mathbf{D}_e^u\right\} \tag{18}$$

where $\left(\mathcal{H}^1(\mathbf{D})\right)^n$ is the space of square integrable n-dimensional vector fields with square integrable first derivatives over the domain $\mathbf{D}$. The weak form of Equation 16 can be recast in a compact for as

$$a(\bar{\boldsymbol{w}}, \bar{\boldsymbol{u}}) = f(\bar{\boldsymbol{w}}), \quad \forall \bar{\boldsymbol{w}} \in \mathcal{V}^0(\mathbf{D}) \tag{19}$$

where the *bilinear form* $a(\bar{\boldsymbol{w}}, \bar{\boldsymbol{u}})$ and the *linear functional* $f(\bar{\boldsymbol{w}})$ have been introduced, defined as

$$a(\bar{\boldsymbol{w}}, \bar{\boldsymbol{u}}) := \int_{\mathbf{D}} \underline{\varepsilon}(\bar{\boldsymbol{w}}) : \left(\hat{\mathbf{E}} : \underline{\varepsilon}(\bar{\boldsymbol{u}})\right) \, \mathrm{d}\mathcal{V} \tag{20}$$

$$f(\bar{\boldsymbol{w}}) := \int_{\partial \mathbf{D}_n} \bar{\boldsymbol{w}} \cdot \bar{\boldsymbol{t}} \, \mathrm{d}\mathcal{S} + \int_{\mathbf{D}} \bar{\boldsymbol{w}} \cdot \bar{\boldsymbol{b}}_V \, \mathrm{d}\mathcal{V} \tag{21}$$

It is worth it to note that the requirement $\bar{\boldsymbol{u}}, \bar{\boldsymbol{w}} \in \left(\mathcal{H}^1(\mathbf{D})\right)^n$ is necessary to bound from above the value of the bilinear form[11].

Introducing the Voigt notation for a plane stress case, the components of the weak form of Equation 19 can be recast as

$$a(\bar{\boldsymbol{w}}, \bar{\boldsymbol{u}}) := \int_{\mathbf{D}} \left([L]\{\bar{\boldsymbol{w}}\}\right)^T [\hat{\mathbf{E}}] \left([L]\{\bar{\boldsymbol{u}}\}\right) \, \mathrm{d}\mathcal{V} \tag{22}$$

$$f(\bar{\boldsymbol{w}}) := \int_{\partial \mathbf{D}_n} \{\bar{\boldsymbol{w}}\}^T \{\bar{\boldsymbol{t}}\} \, \mathrm{d}\mathcal{S} + \int_{\mathbf{D}} \{\bar{\boldsymbol{w}}\}\{\bar{\boldsymbol{b}}_V\} \, \mathrm{d}\mathcal{V} \tag{23}$$

where the derivative operator $[L]$ is such that

$$\{\underline{\varepsilon}(\bar{\boldsymbol{u}})\} = [L]\{\bar{\boldsymbol{u}}\} \rightarrow \begin{pmatrix} \varepsilon_{xx} \\ \varepsilon_{yy} \\ \varepsilon_{xy} \end{pmatrix} = \begin{pmatrix} \partial_x & 0 \\ 0 & \partial_y \\ \partial_y & \partial_x \end{pmatrix} \begin{pmatrix} u_x \\ u_y \end{pmatrix} \tag{24}$$

Within the FEM approach the weak form of Equation 19 is discretised by replacing the trial and test functions $\bar{\boldsymbol{u}}$ and $\bar{\boldsymbol{w}}$ with the approximations $\bar{\boldsymbol{u}}^h \in \mathcal{V}_h(\mathbf{D})$ and $\bar{\boldsymbol{w}}^h \in \mathcal{V}_h^0(\mathbf{D})$, where $\mathcal{V}_h(\mathbf{D})$ and $\mathcal{V}_h^0(\mathbf{D})$ are the *discretised* spaces of trial and test functions such that

$$\mathcal{V}_h(\mathbf{D}) := \left\{\bar{\boldsymbol{u}} \in \left(\mathcal{H}_h^1(\mathbf{D})\right)^n \mid \bar{\boldsymbol{u}} = \bar{\boldsymbol{u}}^* \text{ at } \partial \mathbf{D}_e^u\right\} \tag{25}$$

$$\mathcal{V}_h^0(\mathbf{D}) := \left\{\bar{\boldsymbol{w}} \in \left(\mathcal{H}_h^1(\mathbf{D})\right)^n \mid \bar{\boldsymbol{w}} = 0 \text{ at } \partial \mathbf{D}_e^u\right\} \tag{26}$$

where $\left(\mathcal{H}_h^1(\mathbf{D})\right)^n$ is the space of square integrable n-dimensional *discretised* vector fields (i.e. constructed with approximation functions in terms of a set of nodal parameters) with square integrable first derivatives over the domain $\mathbf{D}$. The discretisation results in a matrix system of the kind

$$[K]\,\{X\} = \{R\} \tag{27}$$

where $[K]$ is the global stiffness matrix of the system, $\{X\}$ the nodal parameters vector collecting all the nodal parameters $\{d_i\}$, and $\{R\}$ the vector of nodal forces. In a FEM model, the stiffness matrix $[K]$ would be evaluated through the contribution of each finite element:

$$[K]_{el} = \int_{\mathbf{D}_{el}} [B(p)]^T [\hat{\mathbf{E}}(p)][B(p)] \, \mathrm{d}\mathcal{V} \tag{28}$$

where the symbol $\int_{\mathbf{D}_{el}}$ indicates the integral over an element, and where the matrix $[B(p)]$ is composed by the submatrices $[B_i(p)]$ as $[B(p)] = ([B_1(p)] \dots [B_i(p)] \dots [B_N(p)])$, such that

$$\{\underline{\varepsilon}(p)\} = \sum_{i=1}^{N} [B_i(p)]\{d_i\} = \begin{pmatrix} \partial_x N_i(p) & 0 \\ 0 & \partial_y N_i(p) \\ \partial_y N_i(p) & \partial_x N_i(p) \end{pmatrix} \begin{pmatrix} d_{xi}^u \\ d_{yi}^u \end{pmatrix} \tag{29}$$

---

[11] Taking into account the analogy between the bilinear form and the total strain energy of a body it is possible to emphasise that this requirement is necessary to bound from above the strain energy.

The requirement of the approximated field variable to belong to the discretised space $\left(\mathcal{H}_h^1(\mathbf{D})\right)^n$ is satisfied when the approximation is constructed with FEM shape functions, which exhibit a piecewise continuous first derivative that is *bounded in an integral sense*. This requirement however, poses a limitation on the use of the meshless shape functions generated with the PIM and RPIMp strategies. Since such shape functions are, in general, *incompatible*, also the resulting approximation of the field variable will be *incompatible*, i.e. it will present *discontinuities*. Hence, if the trial and test functions $\bar{\boldsymbol{u}}$ and $\bar{\boldsymbol{w}}$ are replaced by the approximations $\bar{\boldsymbol{u}}^h$ and $\bar{\boldsymbol{w}}^h$ obtained with PIM or RPIM shape functions, the requirement on the square integrable first derivative won't be satisfied anymore.

3.2.2 Smoothing domains creation

G-spaces are defined for discrete models, where the field variables are expressed in terms of approximation functions and nodal parameters, like the space $\left(\mathcal{H}_h^1(\mathbf{D})\right)^n$ containing the approximated field variables of an FEM model as pointed out in the previous section. Before recalling the definition of G-spaces is then necessary to present the peculiar discretisation strategy which they rely on.

As pointed out in Liu [2010a], the domain $\mathbf{D}$ is discretised with a set of N_e non-overlapping *background cells* $\mathbf{D}_i^C$, with $i = 1, \ldots, N_e$, which vertices correspond to a set of N_n scattered nodes; these cells are, in general, triangular. It is worth it to note that, if one of the T-schemes illustrated in Figure 7 is adopted, the boundaries $\partial\mathbf{D}_i^C$ of the cells represent parts of the domain where the approximation functions may be discontinuous. A further tessellation of the domain is performed, introducing a set of N_S non-overlapping *smoothing domains* $\partial\mathbf{D}_k^S$, with $k = 1, \ldots, N_S$. When generating this second subdivision, the following *no-sharing rule* must be considered: the boundaries $\partial\mathbf{D}_k^S$ of the smoothing domains must not share any finite portion with the boundaries $\partial\mathbf{D}_i^C$ of the background cells, i.e. they may share at most a finite number of points with the parts of the domain where the approximation functions may be discontinuous. The reason for this requirement is to guarantee the possibility to perform the integration of the approximation functions along the boundary of the smoothing domains.

In this treatise, two different strategies for the creation of smoothing domains are considered:

- the *node-based smoothed point interpolation method* (NS-PIM), and
- the *edge-based smoothed point interpolation method* (ES-PIM).

The *node-based smoothed point interpolation method* (NS-PIM) was originally proposed by Liu and his co-authors in Liu et al. [2005], Liu and Zhang [2007], and Zhang et al. [2007] as a meshfree method based on *point interpolation* shape functions with a *nodal integration procedure*[12], and was later shown to belong to the more general class of methods obtained with a *gradient smoothing technique* [Liu, 2008]. Such method relies on the weakened-weak form presented in Section 3.2.5 and, as anticipated by its name, on smoothing domains based on the scattered nodes of the discrete model. Despite it could be used also for one- and three-dimensional problems, in the following attention is focused on the two-dimensional case. The generation of smoothing domains with the *equally-shared smoothing domains strategy*[13] (see, e.g. Liu and Zhang [2013]) is depicted in Figure 8, for an *internal* and a *boundary* domains. The generic smoothing domain $\mathbf{D}_k^S$ at the node k is generated using the surrounding triangular cells, by connecting sequentially, the midpoints of

---

[12] In the cited papers the method was originally called *linearly conforming point interpolation method* (LC-PIM).

[13] The equally-shared smoothing domain strategy is the most common in the NS-PIM. However, as pointed out in Liu and Zhang [2013], for example, also Voronoi cells can be used as smoothing domains, as done in Chen et al. [2001] for the nodal integration strategy in the EFG method.

the cells edges containing the node k with the centroids of the cells. With this strategy, the number of smoothing domains is equal to the number of nodes ($N_S = N_n$), which satifies the minimum number requirement discussed in Liu [2008]. From Figure 8 it can be observed that these domains also satisfy the requirements presented in Section 3.2.2, since they are *non-overlapping* and they respect the *no-sharing rule*; indeed, the boundary $\partial \mathbf{D}_k^S$ of a generic smoothing domain doesn't share any finite portion with the edges of the surrounding cells, where the approximation functions may be discontinuous, but share only the midpoint of their edges.

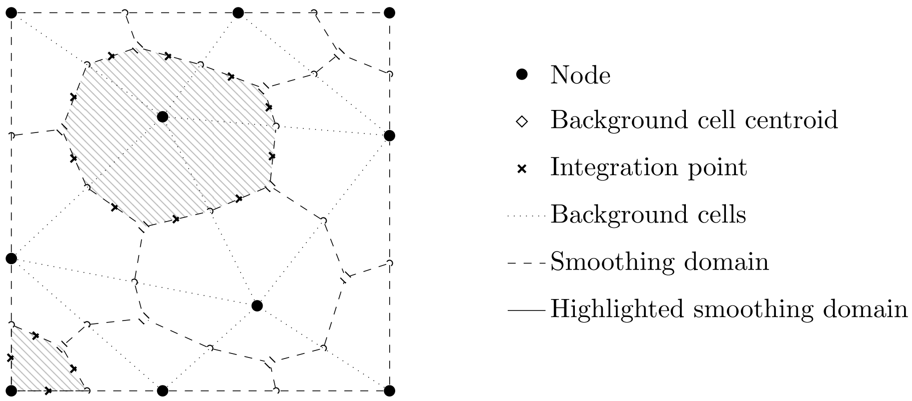

Figure 8: Node-based smoothing domain

The *edge-based smoothed point interpolation method* (ES-PIM) was introduced by Liu and his co-authors in Liu and Zhang [2008] in order to correct the excessive *softnening* effect of the NS-PIM, which resulted in temporally unstable dynamic problems. As pointed out in Liu and Zhang [2013], the ES-PIM exhibits a stiffer behaviour with respect to the NS-PIM, is both spatially and temporally stable, and is capable to produce much more accurate results compared to the NS-PIM and the standard FEM.

The difference between the NS-PIM and the ES-PIM relies in the strategy for the generation of the smoothing domains, which in the latter, as anticipated by the name of the method, is based on the *edges* of the background cells instead of the nodes. As illustrated in Figure 9, the smoothing domain associated to aninternal edge is constructed by connecting the two nodes at the ends of the edge with the centroids of the two triangular cells that share the edge. For a boundary edge the procedure is the same, except for the fact that also the edge belongs to the boundary of the smoothing domain. As pointed out in Liu [2009], also this strategy satisfies the requirement on the minimum number of smoothing domains, is *non-overlapping*, and respect the *no-sharing* rule.

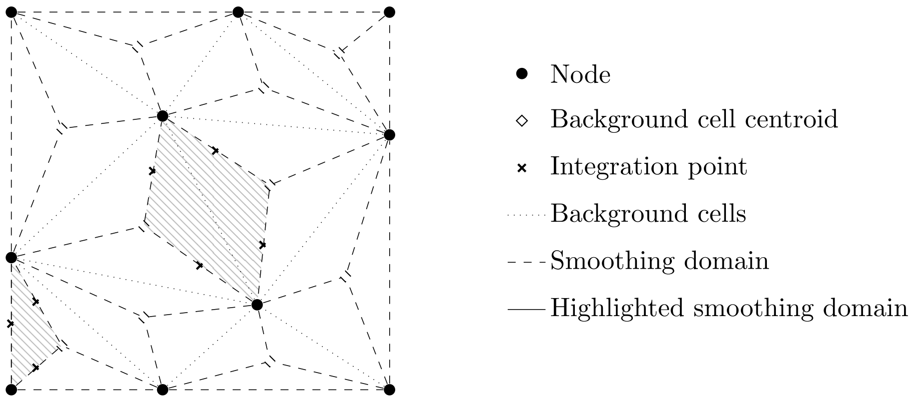

Figure 9: Edge-based smoothing domain

3.2.3 Smoothing operation

The smoothing operation illustrated in this section was introduced by Liu (see, e.g. Liu [2008]) in order to reduce the requirement of continuity of the field variable appearing in the weak form expressed by Equation 16. Such smoothing operation is based on the domain tessellation discussed in Section 3.2.2, assuming the tessellation to be *stationary*[14] during the analysis. Within this approach, the derivative $\mathrm{grad}(\bar{\boldsymbol{u}}) = u_{i,j}\, \bar{\boldsymbol{e}}_i \otimes \bar{\boldsymbol{e}}_j$ of the field variable $\bar{\boldsymbol{u}}$ at a certain point $p \in \mathbf{D}_k^S$ is replaced inside the smoothing domain $\mathbf{D}_k^S$ by the *smoothed derivative* $\widetilde{\mathrm{grad}}(\bar{\boldsymbol{u}}) = \widetilde{u_{i,j}}\, \bar{\boldsymbol{e}}_i \otimes \bar{\boldsymbol{e}}_j$, where

$$u_{i,j}(p) \simeq \widetilde{u_{i,j}}(p_k) := \int_{\mathbf{D}_k^S} u_{i,j}(\xi)\, \widetilde{W}(p_k - \xi)\, \mathrm{d}\mathcal{V}, \quad p \in \mathbf{D}_k^S \tag{30}$$

is *constant* within a smoothing domain. In the equation above, $\widetilde{W}$ is a *smoothing function*, and p_k is the centre of the smoothing domain. If the field variable $\bar{\boldsymbol{u}}$ is continuous, the Green's divergence theorem can be applied, resulting in

$$\widetilde{u_{i,j}}(p_k) = \int_{\partial \mathbf{D}_k^S} \left(u_i(\xi) \otimes n_j^{(k)}(\xi) \right) \widetilde{W}(p_k - \xi)\, \mathrm{d}\mathcal{S} - \int_{\mathbf{D}_k^S} u_i(\xi) \otimes \widetilde{W}_{,j}(p_k - \xi)\, \mathrm{d}\mathcal{V} \tag{31}$$

where $\bar{\boldsymbol{n}}^{(k)}$ is the unitary outward normal vector field on the boundary $\partial \mathbf{D}_k^S$. A common choice for the smoothing function $\widetilde{W}$ is the following Heaviside-type function

$$\widetilde{W}(p_k - \xi) := \begin{cases} 1/A_k & \xi \in \mathbf{D}_k^S \\ 0 & \xi \notin \mathbf{D}_k^S \end{cases} \tag{32}$$

where $A_k = \int_{\mathbf{D}_k^S} \mathrm{d}\mathcal{V}$, which results in

$$\widetilde{u_{i,j}}(p_k) = \frac{1}{A_k} \int_{\partial \mathbf{D}_k^S} u_i(\xi) \otimes n_j^{(k)}(\xi)\, \mathrm{d}\mathcal{S} \tag{33}$$

As pointed out by Liu and Zhang:

> "The "smoothed derivatives" defined in Equation (2.67) [Equation 33 in this treatise] is a generalized concept. It is NOT "the derivative obtained by smoothing the derivatives of the function", because such a gradient does not in general exist, as the function may not be continuous! Rigorously speaking, the "smoothed derivative" is the outward flux of the function across the smoothing domain boundary $\Gamma_{\mathbf{x}}^s$ [$\partial \mathbf{D}_k^S$ in in this treatise]. The smoothed derivative of a function can be approximated using only the function values, and no differentiation is needed. Hence the consistency requirement on the function is reduced, if only the approximate derivative is required." [Liu and Zhang, 2013, pag. 67]

As emphasised in the quoted text, the smoothing operation consists into replace the derivative of the field variable with the smoothed derivative illustrated in Equation 33. This substitution is assumed to be valid whether the field variable is continuous or not, i.e. whether the application of the Green's theorem in Equation 31 is licit or not. As pointed out in Liu [2008], though not rigorous in theory, this operation is possible to implement, since Equation 33 require no differentiation of the field variable, opening the possibility to use PIM and RPIM *incompatible* functions for the approximation of the field variable.

---

[14] The stationarity requirement was originally adopted in Liu [2010a]; however, other *smoothed* methods don't rely on this assumption (see, e.g. Liu and Zhang [2013]).

3.2.4 G-space theory

A general treatement on the G-space theory can be found in Liu [2010a] and Liu and Zhang [2013], and its application to classic elasticity in Liu [2010b]. Briefly, the G-space[15] $\mathcal{G}_h^1(\mathbf{D})$ is defined as the following space of functions $u(p)$ *discretised* in terms of approximation functions $\phi_j(p)$ and nodal parameters d_j

$$\begin{aligned}\mathcal{G}_h^1(\mathbf{D}) := \Big\{ u \mid u(p) = \sum_{j=1}^{N_n} \phi_j(p) d_j,\ u \in \mathcal{L}^2(\mathbf{D}), \\ \sum_{k=1}^{N_S} \left(\int_{\partial \mathbf{D}_k^S} u(\xi)\, n_i^{(k)}(\xi)\, \mathrm{d}\mathcal{S} \right)^2 > 0 \Leftrightarrow u \neq c \in \mathbb{R},\ i = 1, \dots, d \Big\}\end{aligned} \tag{34}$$

where $c \in \mathbb{R}$ is a constant, d the dimension of the space $\mathbf{D}$, and $\mathcal{L}^2(\mathbf{D})$ the *Lebesgue* space of square integrable functions. When n-dimensional vector fields are considered, the following space can be introduced

$$\left(\mathcal{G}_h^1(\mathbf{D})\right)^n := \left\{ \bar{\boldsymbol{u}} = u_i\, \bar{\boldsymbol{e}}_i \mid u_i \in \mathcal{G}_h^1(\mathbf{D}),\ i = 1, \dots, n \right\} \tag{35}$$

This space is endowed with the following *inner product*

$$< \bar{\boldsymbol{u}}, \bar{\boldsymbol{w}} >_{\mathcal{G}^1} = \underbrace{\int_{\mathbf{D}} (\bar{\boldsymbol{u}} \cdot \bar{\boldsymbol{w}})\, \mathrm{d}\mathcal{V}}_{< \bar{\boldsymbol{u}}, \bar{\boldsymbol{w}} >_{\mathcal{L}^2}} + \underbrace{\int_{\mathbf{D}} \left(\widetilde{\mathrm{grad}}(\bar{\boldsymbol{u}}) : \widetilde{\mathrm{grad}}(\bar{\boldsymbol{w}}) \right) \mathrm{d}\mathcal{V}}_{< \widetilde{\mathrm{grad}}(\bar{\boldsymbol{u}}), \widetilde{\mathrm{grad}}(\bar{\boldsymbol{w}}) >_{\mathcal{L}^2}}, \quad \bar{\boldsymbol{u}}, \bar{\boldsymbol{v}} \in \left(\mathcal{G}_h^1(\mathbf{D})\right)^n \tag{36}$$

with induced *norm* $\|\cdot\|_{\mathcal{G}^1}^2$ and *semi-norm* $|\cdot|_{\mathcal{G}^1}^2$ expressed as combination of norms in the Lebesgue space $\mathcal{L}^2(\mathbf{D})$

$$\|\bar{\boldsymbol{u}}\|_{\mathcal{G}^1}^2 = \|\bar{\boldsymbol{u}}\|_{\mathcal{L}^2}^2 + |\bar{\boldsymbol{u}}|_{\mathcal{G}^1}^2, \quad \bar{\boldsymbol{u}} \in \left(\mathcal{G}_h^1(\mathbf{D})\right)^n \tag{37}$$

$$|\bar{\boldsymbol{u}}|_{\mathcal{G}^1}^2 = \left\| \widetilde{\mathrm{grad}}(\bar{\boldsymbol{u}}) \right\|_{\mathcal{L}^2}^2, \quad \bar{\boldsymbol{u}} \in \left(\mathcal{G}_h^1(\mathbf{D})\right)^n \tag{38}$$

As it can be observed in Equation 34, the shape functions must be (i) *linearly independent*, in order to form a basis, (ii) *bounded*, i.e. square integrable, and (iii) must verify the following *positivity condition*:

$$\sum_{k=1}^{N_S} \left(\int_{\partial \mathbf{D}_k^S} u(\xi)\, n_i^{(k)}(\xi)\, \mathrm{d}\mathcal{S} \right)^2 > 0 \tag{39}$$

The two last requirements, as pointed out by Liu [Liu, 2010a], are necessary to guarantee the stability and convergence of the numerical models built upon the weakened-weak formulation based on G-spaces.

The main difference between the space $\mathcal{G}_h^1(\mathbf{D})$ and the space $\mathcal{H}_h^1(\mathbf{D})$ usually adopted in FEM applications (i.e. the discretised space of square integrable functions with square integrable first derivative), is the fact that the latter requires both the function and its first derivative to be square integrable ($\|\bar{\boldsymbol{u}}\|_{\mathcal{L}^2(\mathbf{D})}^2 < \infty$ and $\|\mathrm{grad}(\bar{\boldsymbol{u}})\|_{\mathcal{L}^2(\mathbf{D})}^2 < \infty$) in order to ensure an upper bound to the strain energy (aka the bilinear form), while in the former only the function is required to be square integrable since, as it will be discussed in the following section, the bilinear form of the weakened-weak form depends only on the function and not on its first derivative. While in the weakened-weak form the strain energy is automatically bounded from above once the functions are

---

[15] The more general case of spaces $\mathcal{G}_h^m(\mathbf{D})$ with $m > 1$ is not considered here.

square integrable, a lower bound must be explicitly imposed, with the aforementioned positivity condition; in the standard weak form, as pointed out in Liu [2010a], an explicit lower bound is not necessary, since the condition $\|\mathrm{grad}(\bar{\boldsymbol{u}})\|^2_{\mathcal{L}^2(\mathbf{D})} = 0$ is attained only if the function is zero everywhere, due to the Poincare-Friedrichs inequality[16] [Liu, 2009]. The reduced order of continuity required by the space $\mathcal{G}^1_h(\mathbf{D})$ opens the possibility to use PIM and RPIM shape functions as a basis to generate its elements. The main characteristics of G-spaces needed to guarantee the existence and uniqueness of the solution of the weakened-weak formulation discussed in the following Section 3.2.5 have been widely discussed by Liu and his co-authors in a number of papers and books (see, e.g. Liu [2010a,b, 2009] and Liu and Zhang [2013]) and won't be recalled here.

3.2.5 Weakened-weak form of the classic elasticity problem

The weakened-weak form in classic elasticity have been presented in Liu [2010b]. As discussed in the mentioned paper, such formulation can be obtained by replacing the strain tensor $\underline{\varepsilon}$ appearing in the bilinear form of Equation 20 with its *smoothed* version $\widetilde{\underline{\varepsilon}}$, resulting in the *smoothed bilinear form*

$$\widetilde{a}(\bar{\boldsymbol{w}}, \bar{\boldsymbol{u}}) = \int_{\mathbf{D}} \widetilde{\underline{\varepsilon}}(\bar{\boldsymbol{w}}(p_k)) : \left(\hat{\mathbf{E}} : \widetilde{\underline{\varepsilon}}(\bar{\boldsymbol{u}}(p_k))\right) \, \mathrm{d}\mathcal{V} \tag{40}$$

where the smoothed strain tensor $\widetilde{\underline{\varepsilon}}$ is obtained considering the smoothing derivatives of Equation 33

$$\widetilde{\varepsilon}_{ij} = \frac{1}{2}\left(\widetilde{u_{i,j}} + \widetilde{u_{j,i}}\right) \tag{41}$$

In plane stress case, the strain tensor assumes the following matrix expression:

$$\{\widetilde{\underline{\varepsilon}}(\bar{\boldsymbol{u}}(p_k))\} = \frac{1}{A_k}\int_{\partial\mathbf{D}^S_k} [\widetilde{L_n}(\xi)]\{\bar{\boldsymbol{u}}(\xi)\} \, \mathrm{d}\mathcal{S} \tag{42}$$

$$\begin{pmatrix} \widetilde{\varepsilon}_{xx} \\ \widetilde{\varepsilon}_{yy} \\ \widetilde{\varepsilon}_{xy} \end{pmatrix} = \frac{1}{A_k}\int_{\partial\mathbf{D}^S_k} \begin{pmatrix} n^{(k)}_x(\xi) & 0 \\ 0 & n^{(k)}_y(\xi) \\ n^{(k)}_y(\xi) & n^{(k)}_x(\xi) \end{pmatrix} \begin{pmatrix} u_x(\xi) \\ u_y(\xi) \end{pmatrix} \mathrm{d}\mathcal{S} \tag{43}$$

Recalling that the smoothed derivatives are *constant* within each smoothing domain defined in Section 3.2.2, and also assuming the constitutive operator $\hat{\mathbf{E}}$ to be constant within each smoothing domain, the integral $\int_{\mathbf{D}}$ may be replaced with a summation over the smoothing domains, resulting in

$$\widetilde{a}(\bar{\boldsymbol{w}}, \bar{\boldsymbol{u}}) = \sum_{k=1}^{N_S} A_k \left(\widetilde{\underline{\varepsilon}}(\bar{\boldsymbol{w}}(p_k)) : \left(\hat{\mathbf{E}} : \widetilde{\underline{\varepsilon}}(\bar{\boldsymbol{u}}(p_k))\right)\right) \tag{44}$$

The *weakened-weak form* of the classic elasticity problem recalled in Section 3.2.1 consists then into find the field $\bar{\boldsymbol{u}} \in \mathcal{V}(\mathbf{D})$ such that

$$\widetilde{a}(\bar{\boldsymbol{w}}, \bar{\boldsymbol{u}}) = f(\bar{\boldsymbol{w}}), \quad \forall \bar{\boldsymbol{w}} \in \mathcal{V}^0(\mathbf{D}) \tag{45}$$

where $\mathcal{V}(\mathbf{D})$ and $\mathcal{V}^0(\mathbf{D})$ are, respectively, the spaces of *trial* and *test* functions, defined as

$$\mathcal{V}(\mathbf{D}) := \left\{\bar{\boldsymbol{u}} \in \left(\mathcal{G}^1_h(\mathbf{D})\right)^n \mid \bar{\boldsymbol{u}} = \bar{\boldsymbol{u}}^* \text{ at } \partial\mathbf{D}^u_e\right\} \tag{46}$$

$$\mathcal{V}^0(\mathbf{D}) := \left\{\bar{\boldsymbol{w}} \in \left(\mathcal{G}^1_h(\mathbf{D})\right)^n \mid \bar{\boldsymbol{w}} = 0 \text{ at } \partial\mathbf{D}^u_e\right\} \tag{47}$$

---

[16] As pointed out in Liu [2009], the Poincare-Friedrichs inequality is represented by $c\|\bar{\boldsymbol{w}}\|^2_{\mathcal{H}^1} \leq |\bar{\boldsymbol{w}}|^2_{\mathcal{H}^1}$, $\forall\, \bar{\boldsymbol{w}} \in \left(\mathcal{H}^1_0(\mathbf{D})\right)^k$, with $c \in \mathbb{R}$ and $c > 0$, and expresses an equivalence between the norm and the seminorm for k-dimensional vector fields in the space $\mathcal{H}^1_0(\mathbf{D})$ of square integrable k-dimensional vector fields with square integrable first derivative with prevented *rigid-body* motions.

Discussions on the properties of the weakened-weak form of Equation 45, as well as on the conditions that ensure the existence and uniqueness of the solution $\bar{\boldsymbol{u}} \in \mathcal{V}(\mathbf{D})$ can be found in Liu and Zhang [2008] and Liu [2010b].

The absence of derivatives in the smoothed bilinear form (Equation 44) allows to express both the trial and the test functions in terms of PIM and RPIM shape functions $\phi_i(p)$, since they are well suited to form a basis for the space $\left(\mathcal{G}_h^1(\mathbf{D})\right)^n$, resulting (for the trial functions) in

$$\{\bar{\boldsymbol{u}}(p)\} = \sum_{i \in S_d} [\phi_i(p)]\{d_i\} \tag{48}$$

where $\{d_i\}$ is the array collecting the nodal parameters at the node i, and where S_d is the support domain of the point $p \in \mathbf{D}$. The smoothed strains can be expressed in terms of the smoothed strain-displacement matrix $[\widetilde{B}_i(p_k)]$ as

$$\{\widetilde{\boldsymbol{\varepsilon}}(\bar{\boldsymbol{u}}(p_k))\} = \sum_{i \in S_d} [\widetilde{B}_i(p_k)]\{d_i\} \tag{49}$$

where $[\widetilde{B}_i(p_k)]$, in a plane stress state, is represented by

$$\begin{aligned}
[\widetilde{B}_i(p_k)] &= \frac{1}{A_k} \int_{\partial \mathbf{D}_k^S} [\widetilde{L_n}(\xi)][\phi_i(\xi)] \, \mathrm{d}\mathcal{S} \\
&= \frac{1}{A_k} \int_{\partial \mathbf{D}_k^S} \begin{pmatrix} n_x^{(k)}(\xi)\, \phi_i(\xi) & 0 \\ 0 & n_y^{(k)}(\xi)\, \phi_i(\xi) \\ n_y^{(k)}(\xi)\, \phi_i(\xi) & n_x^{(k)}(\xi)\, \phi_i(\xi) \end{pmatrix} \mathrm{d}\mathcal{S} \\
&= \begin{pmatrix} \widetilde{\phi}_{i,x}(p_k) & 0 \\ 0 & \widetilde{\phi}_{i,y}(p_k) \\ \widetilde{\phi}_{i,y}(p_k) & \widetilde{\phi}_{i,x}(p_k) \end{pmatrix}
\end{aligned} \tag{50}$$

where the terms $\widetilde{\phi}_{i,l}(p_k)$ are the *smoothed* derivatives of the shape functions, expressed by

$$\widetilde{\phi}_{i,l}(p_k) := \frac{1}{A_k} \int_{\partial \mathbf{D}_k^S} n_l^{(k)}(\xi)\, \phi_i(\xi) \, \mathrm{d}\mathcal{S}, \quad l = x, y \tag{51}$$

The smoothed shape functions appearing in Equation 51, which allow to evaluate the smoothed bilinear form, are calculated performing a numerical integration along the boundary $\partial \mathbf{D}_k^S$ of each smoothing domain. Since the boundary of each smoothing domain is composed by a set of linear segments, the integration can be expressed as a sum of Gaussian quadratures over each segment, resulting in

$$\widetilde{\phi}_{i,l}(p_k) = \frac{1}{A_k} \sum_{m=1}^{n_{seg}} \frac{L_m}{2} \left(\sum_{n=1}^{n_{gp}} W_n^{gp}\, \phi_i(p_{m,n})\, n_{l,m}^{(k)} \right), \quad l = x, y \tag{52}$$

where n_{seg} is the number of segments, L_m the length of the *m-th* segment, n_{gp} the number of integration points of each segment, $p_{m,n}$ the *n-th* integration point of the *m-th* segment with associated weight W_n^{gp}, and $n_{l,m}^{(k)}$ the component in the direction l of the unit normal to the *m-th* segment of the *k-th* smoothing domain.

Finally, the discretisation results in the same algebraic system expressed in Equation 27, where now the stiffness matrix $[K]$ is evaluated in terms the contribution of each *smoothing domain*

$$[K(p_k)]_{Sd} = A_k [\widetilde{B}(p_k)]^T [\hat{\mathbf{E}}(p_k)][\widetilde{B}(p_k)] \tag{53}$$

where, as in the FEM, the matrix $[\widetilde{B}(p_k)]$ is composed by the submatrices $[\widetilde{B}_i(p_k)]$ as:

$$[\widetilde{B}(p_k)] = \Big([\widetilde{B}_1(p_k)]\dots[\widetilde{B}_i(p_k)]\dots[\widetilde{B}_N(p_k)]\Big) \tag{54}$$

where N is the number of nodes in the support domain S_d at the point p_k.

Due to the peculiar domain tessellation and to the adoption of the smoothing operation, SPIM models exhibit different properties when compared to the standard FEM. In Liu and Zhang [2007] and Liu [2008], the authors pointed out that the smoothed bilinear form is capable to provide *softer* results with respect to the standard weak form, when the same approximation functions are used ($\widetilde{a}(\bar{\boldsymbol{w}},\bar{\boldsymbol{w}}) \leq a(\bar{\boldsymbol{w}},\bar{\boldsymbol{w}}), \bar{\boldsymbol{w}} \in \mathcal{V}_h^0(\mathbf{D})$). They also showed that it is also capable to provide an *upper bound* approximation to the exact solution. This last characteristic however, depends on both the kind of approximation functions that are being adopted, and on the peculiar strategy used for the generation of the smoothing domains.

3.3 SPIMs for damage modelling

The first application of SPIM strategies to the modelling of damage problems was proposed by Gori et al. [2019b], where the authors also pointed out the regularisation properties induced by the SPIM approach; later, in Saliba et al. [2021], a strategy was proposed to analyse damage models with a coupled SPIM-FEM model. Some of the results discussed in Gori et al. [2019b] are recalled in this section.

Here, attention is focused on the case of *scalar-isotropic damage models* in a geometrically linear context. Such models belong to the more general class of elastic-degrading models, and are expressed in terms of a *secant* stress-strain relation $\underline{\boldsymbol{\sigma}} = \hat{\mathbf{E}}^S : \underline{\boldsymbol{\varepsilon}}$, where $\hat{\mathbf{E}}^S$ is the *secant* constitutive operator, which components depend both on the *initial* constitutive tensor $\hat{\mathbf{E}}$ and on a *scalar damage variable* D, assuming values from 0 to 1. When the damage is assumed to be *isotropic* the secant constitutive operator is represented by the well-known expression $\hat{\mathbf{E}}^S(D, \hat{\mathbf{E}}) = (1-D)\,\hat{\mathbf{E}}$. In such models the loading process is represented in terms of a loading function which is usually expressed as the following additive decomposition:

$$f(\underline{\boldsymbol{\varepsilon}}, D) = \varepsilon_{eq}(\underline{\boldsymbol{\varepsilon}}) - K(D) \leq 0 \tag{55}$$

where $\varepsilon_{eq}(\underline{\boldsymbol{\varepsilon}})$ is a function depending only on the strain tensor, usually indicated as *equivalent deformation*, that represents the loading condition of the continuum, while $K(D)$ is a *historical parameter* that depends only on the damage variable and that is representative of the maximum level of deformation reached during the loading process. The rate of the previous secant relation, $\dot{\underline{\boldsymbol{\sigma}}} = \hat{\mathbf{E}}^S : \dot{\underline{\boldsymbol{\varepsilon}}} + \dot{\hat{\mathbf{E}}}^S : \underline{\boldsymbol{\varepsilon}}$, can be recast in the *tangent* relation $\dot{\underline{\boldsymbol{\sigma}}} = \hat{\mathbf{E}}^t : \dot{\underline{\boldsymbol{\varepsilon}}}$ between the stress and the strain rates, where $\hat{\mathbf{E}}^t$ is the tangent constitutive operator expressed by Carol et al. [1994]

$$\hat{\mathbf{E}}^t = (1-D)\,\hat{\mathbf{E}} - \frac{1}{H^*}\left(\underline{\boldsymbol{m}}^* \otimes \underline{\boldsymbol{n}}^*\right) \tag{56}$$

where

$$\underline{\boldsymbol{m}}^* := -\hat{\mathbf{E}} \cdot \underline{\boldsymbol{\varepsilon}}, \qquad \underline{\boldsymbol{n}}^* := \frac{\partial \varepsilon_{eq}}{\partial \underline{\boldsymbol{\varepsilon}}}, \qquad H^* := \frac{\partial K(D)}{\partial D} = \left(\frac{\partial D(\varepsilon_{eq})}{\partial \varepsilon_{eq}}\right)^{-1} \tag{57}$$

The function $D(\varepsilon_{eq})$ is a prescribed damage evolution law; in the numerical examples of Section 5, the following exponential damage law was considered:

$$D(\varepsilon_{eq}) = 1 - \frac{K_0}{\varepsilon_{eq}}\left(1 - \alpha + \alpha e^{-\beta(\varepsilon_{eq} - K_0)}\right) \tag{58}$$

In the expression above, K_0 is a threshold value for the equivalent deformation, representing the onset of damage, and where α and β are parameters that define, respectively, the maximum allowed damage level and the damage evolution intensity. Different scalar damage models can be obtained choosing a peculiar equivalent deformation; in the numerical examples of Section 5, the following equivalent deformation by *Mazars* [Mazars, 1984, de Borst and Gutiérrez, 1999] was adopted:

$$\varepsilon_{eq} = \sqrt{\left[\sum_{k=1}^{3} \left(< \varepsilon^{(k)} >_+\right)^2\right]} \tag{59}$$

where $\varepsilon^{(k)}$ the k-th eigenvalue of the strain tensor, and $< \varepsilon^{(k)} >_+ = (\varepsilon^{(k)} + |\varepsilon^{(k)}|)/2$ its positive part.

As discussed by Gori et al. [2019b], the main issue for the application of SPIM strategies to elastic-degradation is the transition from Eq. 40 to Eq. 44, i.e. the passage from a smoothed bilinear form expressed in terms of the domain integral $\int_{\mathbf{D}}$ to a smoothed bilinear form expressed as a summation over the number of smoothing domains, that relies on the assumption of a linear elastic constitutive operator $\hat{\mathbf{E}}$ *constant* within a smoothing domain. In a physically linear problem, since the material properties are independent on the state of the body, this assumption is verified both in case of homogeneous and heterogeneous materials; an eventual heterogeneous distribution of the material properties indeed, could be easily considered with the attribution of different material properties at each smoothing domain, constant over the same smoothing domain.

When dealing with elastic-degrading models, the initial elastic constitutive operator $\hat{\mathbf{E}}$ appearing in the smoothed bilinear form (Eq. 40) must be replaced with the *secant* operator $\hat{\mathbf{E}}^S$, which depends on the state of the body, and which varies during the loading process:

$$\widetilde{a}(\bar{\boldsymbol{w}}, \bar{\boldsymbol{u}}) = \int_{\mathbf{D}} \widetilde{\underline{\varepsilon}}(\bar{\boldsymbol{w}}(p_k)) : \left(\hat{\mathbf{E}}^S(\underline{\varepsilon}(\bar{\boldsymbol{u}})) : \widetilde{\underline{\varepsilon}}(\bar{\boldsymbol{u}}(p_k))\right) \, \mathrm{d}\mathcal{V} \tag{60}$$

In order to obtain an expression similar to the second one of Eq. 44, a *smoothed* constitutive operator $\widetilde{\hat{\mathbf{E}}^S}(p_k)$, *constant* over the smoothing domain $\mathbf{D}_k^S$, must be introduced, resulting in

$$\widetilde{a}(\bar{\boldsymbol{w}}, \bar{\boldsymbol{u}}) = \sum_{k=1}^{N_S} A_k \left(\widetilde{\underline{\varepsilon}}(\bar{\boldsymbol{w}}(p_k)) : \left(\widetilde{\hat{\mathbf{E}}^S}(p_k) : \widetilde{\underline{\varepsilon}}(\bar{\boldsymbol{u}}(p_k))\right)\right) \tag{61}$$

Regarding how to obtain such smoothed constitutive operator it can be observed that the secant operator depends on the state of the body at each point $\xi \in \mathbf{D}_k^S$, i.e. on the current strain tensor $\underline{\varepsilon}(\bar{\boldsymbol{u}}(\xi))$ which depends on the displacement field. In NS-PIM and ES-PIM procedures, the displacement field is calculated at the point p_k of each smoothing domain $\mathbf{D}_k^S$, resulting in a smoothed strain tensor $\widetilde{\underline{\varepsilon}}(\bar{\boldsymbol{u}}(p_k))$ which is constant within a smoothing domain. The smoothed constitutive operator can then be approximated with the secant operator generated using the smoothed strain as

$$\widetilde{\hat{\mathbf{E}}^S}(p_k) \simeq \hat{\mathbf{E}}^S(\widetilde{\underline{\varepsilon}}(\bar{\boldsymbol{u}}(p_k)) \tag{62}$$

resulting in

$$\widetilde{a}(\bar{\boldsymbol{w}}, \bar{\boldsymbol{u}}) = \sum_{k=1}^{N_S} A_k \left(\widetilde{\underline{\varepsilon}}(\bar{\boldsymbol{w}}(p_k)) : \left(\hat{\mathbf{E}}^S(\widetilde{\underline{\varepsilon}}(\bar{\boldsymbol{u}}(p_k)) : \widetilde{\underline{\varepsilon}}(\bar{\boldsymbol{u}}(p_k))\right)\right) \tag{63}$$

In the specific case of a scalar-isotropic damage models the secant constitutive operator depends on the scalar damage variable D which, according to Eq. 58, can be expressed as a function that depends on the current strain state of the body through an equivalent strain measure, $D = D(\varepsilon_{eq})$

with $\varepsilon_{eq} = \varepsilon_{eq}(\underline{\varepsilon}(\bar{\boldsymbol{u}}(p)))$. In this case, the smoothed constitutive operator will depend on the smoothed damage variable $\widetilde{D}(p_k)$, depending on the smoothed equivalent strain measure $\widetilde{\varepsilon}_{eq}$ as

$$\widetilde{\hat{\mathbf{E}}^S}(p_k) = (1 - \widetilde{D}(p_k))\,\hat{\mathbf{E}}, \quad \widetilde{D}(p_k) = D(\widetilde{\varepsilon}_{eq}), \quad \widetilde{\varepsilon}_{eq} = \varepsilon_{eq}(\widetilde{\underline{\varepsilon}}(\bar{\boldsymbol{u}}(p_k))) \tag{64}$$

3.4 Linearisation of the weakened-weak form

In presence of damage, the algebraic systems of Eq. 27 must be recast as the following nonlinear system:

$$[K^S]\,\{X\} = \{R\} \tag{65}$$

where $[K]^S$ is the global secant stiffness matrix of the discrete model, resulting from the discretisation of the smoothed bilinear form of Eq. 63. This nonlinear system can be solved with an incremental-iterative strategy based on the *Newton-Raphson* method, which requires the *linearisation* of Eq. 65, as in the standard nonlinear FEM [Wriggers, 2008].

The first step for the linearisation within the Newton-Raphson method consists in the introduction of a space of *admissible variations* $\delta\mathcal{V}(\mathbf{D})$, associated with the space of trial functions $\mathcal{V}(\mathbf{D})$, defined as

$$\delta\mathcal{V}(\mathbf{D}) := \left\{\delta\bar{\boldsymbol{u}} \in \left(\mathcal{G}^1_h(\mathbf{D})\right)^n \mid \delta\bar{\boldsymbol{u}} = \bar{\mathbf{0}} \text{ at } \partial\mathbf{D}^u_e\right\} \tag{66}$$

The admissible variations $\delta\bar{\boldsymbol{u}}$ allow to obtain a set of *perturbed* configurations $\mathcal{V}_\varepsilon(\mathbf{D})$, whose elements $\bar{\boldsymbol{u}}_\varepsilon = \bar{\boldsymbol{u}} + \varepsilon\,\delta\bar{\boldsymbol{u}}$ satisfy the kinematical boundary conditions of the problem prescribed at $\partial\mathbf{D}^u_e$. The weakened-weak form of Eq. 45 can be recast as

$$G(\bar{\boldsymbol{w}}, \bar{\boldsymbol{u}}) := \widetilde{a}(\bar{\boldsymbol{w}}, \bar{\boldsymbol{u}}) - f(\bar{\boldsymbol{w}}) = 0, \quad \forall\bar{\boldsymbol{w}} \in \mathcal{V}^0(\mathbf{D}) \tag{67}$$

with the introduction of the functional $G(\bar{\boldsymbol{w}}, \bar{\boldsymbol{u}})$. In order to obtain a linearisation of such functional, a *perturbed* configuration $G(\bar{\boldsymbol{w}}, \bar{\boldsymbol{u}}_\varepsilon)$ near the *known* equilibrium configuration $G(\bar{\boldsymbol{w}}, \bar{\boldsymbol{u}})$ (which satisfies Eq. 67) is introduced; such perturbed configuration must satisfy the condition

$$G(\bar{\boldsymbol{w}}, \bar{\boldsymbol{u}}_\varepsilon) = \widetilde{a}(\bar{\boldsymbol{w}}, \bar{\boldsymbol{u}}_\varepsilon) - f(\bar{\boldsymbol{w}}) = 0, \quad \forall\bar{\boldsymbol{w}} \in \mathcal{V}^0(\mathbf{D}) \tag{68}$$

The vector field $\delta\bar{\boldsymbol{u}}$ which allows to reach the new equilibrium configuration can be calculated with the linearisation $G(\bar{\boldsymbol{w}}, \bar{\boldsymbol{u}}_\varepsilon) \simeq L\left[G(\bar{\boldsymbol{w}}, \bar{\boldsymbol{u}}_\varepsilon)\right]$, resulting in

$$L\left[G(\bar{\boldsymbol{w}}, \bar{\boldsymbol{u}}_\varepsilon)\right] = G(\bar{\boldsymbol{w}}, \bar{\boldsymbol{u}}) + DG(\bar{\boldsymbol{w}}, \bar{\boldsymbol{u}}) \cdot \delta\bar{\boldsymbol{u}} = 0, \quad \forall\bar{\boldsymbol{w}} \in \mathcal{V}^0(\mathbf{D}) \tag{69}$$

where the terms $DG(\bar{\boldsymbol{w}}, \bar{\boldsymbol{u}}_\varepsilon) \cdot \delta\bar{\boldsymbol{u}}$ is the following *directional* (or *Fréchet*) derivative

$$DG(\bar{\boldsymbol{w}}, \bar{\boldsymbol{u}}) \cdot \delta\bar{\boldsymbol{u}} = \left.\frac{\partial G(\bar{\boldsymbol{w}}, \bar{\boldsymbol{u}}_\varepsilon)}{\partial\varepsilon}\right|_{\varepsilon=0} \tag{70}$$

that can be shown to be expressed by

$$\begin{aligned} DG(\bar{\boldsymbol{w}}, \bar{\boldsymbol{u}}) \cdot \delta\bar{\boldsymbol{u}} &= \sum_{k=1}^{N_S} A_k \left(\widetilde{\underline{\varepsilon}}(\bar{\boldsymbol{w}}(p_k)) : \left(\hat{\mathbf{E}}^t(\widetilde{\underline{\varepsilon}}(\bar{\boldsymbol{u}}(p_k)) : \delta\widetilde{\underline{\varepsilon}}(\bar{\boldsymbol{u}}(p_k))\right)\right) \\ &= \sum_{k=1}^{N_S} A_k \left(\widetilde{\underline{\varepsilon}}(\bar{\boldsymbol{w}}(p_k)) : \left(\hat{\mathbf{E}}^t(\widetilde{\underline{\varepsilon}}(\bar{\boldsymbol{u}}(p_k)) : \dot{\widetilde{\underline{\varepsilon}}}(\bar{\boldsymbol{u}}(p_k))\right)\right) \end{aligned} \tag{71}$$

where the admissible variation of the smoothed strain tensor ($\delta\widetilde{\underline{\varepsilon}}$) coincides with its rate ($\dot{\widetilde{\underline{\varepsilon}}}$), and where the tangent constitutive operator $\hat{\mathbf{E}}^t$ is the one defined in Eq. 56 (see Gori et al. [2019b] for further details). The linearised weakened-weak form can then be recast into: find the *increments* $\delta\bar{\boldsymbol{u}} \in \delta\mathcal{V}(\mathbf{D})$ such that

$$DG(\bar{\boldsymbol{w}}, \bar{\boldsymbol{u}}) \cdot \delta\bar{\boldsymbol{u}} = -G(\bar{\boldsymbol{w}}, \bar{\boldsymbol{u}}), \quad \forall \bar{\boldsymbol{w}} \in \mathcal{V}^0(\mathbf{D}) \tag{72}$$

The right hand side of Eq. 72 is known, since it depends on the displacement field $\bar{\boldsymbol{u}}$ of a known equilibrium configuration, and is expressed as

$$G(\bar{\boldsymbol{w}}, \bar{\boldsymbol{u}}) = \widetilde{a}(\bar{\boldsymbol{w}}, \bar{\boldsymbol{u}}) - f(\bar{\boldsymbol{w}}) = \sum_{k=1}^{N_S} A_k \left(\underline{\widetilde{\varepsilon}}(\bar{\boldsymbol{w}}(p_k)) : \underline{\widetilde{\boldsymbol{\sigma}}}(\bar{\boldsymbol{u}}(p_k)) \right) - f(\bar{\boldsymbol{w}}) \tag{73}$$

Introducing PIM or RPIM approximation functions into Eq. 72, for both the test functions $\bar{\boldsymbol{w}}(p)$ and the increments $\delta\bar{\boldsymbol{u}}(p)$:

$$\{\bar{\boldsymbol{w}}(p)\} = \sum_{i \in S_d} [\phi_i(p)]\{d_i^w\}, \quad \{\delta\bar{\boldsymbol{u}}(p)\} = \sum_{i \in S_d} [\phi_i(p)]\{\delta d_i\} \tag{74}$$

the following algebraic system can be obtained

$$[K^t]\,\{\Delta X\} = \{N\} \tag{75}$$

where $[K^t]$ is the global *tangent* stiffness matrix of the discrete model, $\{\Delta X\}$ the nodal parameters vector collecting all the nodal parameters $\{\delta d_i\}$, and $\{N\}$ an array containing the discretisation of the right hand side of Eq. 72. The matrix $[K^t]$ is evaluated through the contribution of each *smoothing domain*

$$[K^t(p_k)]_{Sd} = A_k [\widetilde{B}(p_k)]^T [\hat{\mathbf{E}}^t(\underline{\widetilde{\varepsilon}}(\bar{\boldsymbol{u}}(p_k)))][\widetilde{B}(p_k)] \tag{76}$$

where as in the linear SPIM, the matrix $[\widetilde{B}(p_k)]$ is composed by the submatrices $[\widetilde{B}_i(p_k)]$ as $[\widetilde{B}(p_k)] = \Big([\widetilde{B}_1(p_k)] \ldots [\widetilde{B}_i(p_k)] \ldots [\widetilde{B}_N(p_k)]\Big)$, where N is the number of nodes in the support domain S_d at the point p_k, and where $[\hat{\mathbf{E}}^t(\underline{\widetilde{\varepsilon}}(\bar{\boldsymbol{u}}(p_k)))]$ is the matricial expression of the tangent constitutive operator of Eq. 56.

4 Regularisation strategies for damage models

As already stated in Section 1, the objective of this manuscript is to discuss the application of SPIM strategies to the analysis of damage models, taking advantage of the regularisation effects provided by the intrinsic nonlocal character of such formulations. Damage models and other strain-softening models are characterised by the phenomenon of *localisation*, and when analised with the standard FEM they may exhibit certain pathological behaviours such as *strong mesh-dependency*, *premature fracture initiation*, and *instantaneous perfectly-brittle fracture* [de Borst et al., 1993, Peerlings et al., 2002], as already discussed in Section 1. As pointed out in the literature (see, e.g. the paper by Bažant [Bažant, 1991]), these pathological behaviours are due to the *local* representation offered by the classic continuum theory, in contrast with the *nonlocal* nature of phenomena like damage and plasticity. The main aim of the proposed solutions to this problem, the so-called *regularisation* techniques, is the introduction of an *internal length* in the continuum model, allowing to recover the nonlocal character of the phenomenon.

Regularisation techniques may act on two different levels: at the *formulation* level, i.e. directly in the continuum description, or at the *numerical* level, i.e. within the discretisation method. Among the different alternatives for regularisation at the formulation level there are: *nonlocal* and *gradient-enhanced* models [Bažant and Lin, 1988, Pijaudier-Cabot and Bažant, 1987, de Borst and Mühlhaus, 1992, Peerlings et al., 1996, 2001, 2002, Badnava et al., 2016], *viscous* models

[Needleman, 1988], *cohesive zone* models [Dugdale, 1960, Barenblatt, 1962], methods based on the *fracture energy approach* [Bažant and Oh, 1983], *phase-field* models [Frémond and Nedjar, 1996, Miehe et al., 2010, 2016], and the *micropolar* theory [de Borst, 1991, de Borst and Sluys, 1991, Dietsche et al., 1993, Iordache and Willam, 1998, Xotta et al., 2016, Gori et al., 2017b,a, Gori, 2018]. The micropolar theory has been used in combination with the SPIM approach in the numerical simulations of Section 5.3, in order to obtain a two-levels regularisation strategy (for more details on the application of the micropolar theory to damage models and it's combination with the SPIM strategy refer to the papers by Gori et al. [Gori et al., 2017a,b, 2019c]).

Regularisation techniques at the numerical level can be based on the FEM or on other discretisation methods. Among the various solutions based on the finite element method there are, for example, the use of elements with embedded discontinuities [Ortiz et al., 1987], able to represent various kind of weak and strong discontinuities, or element with embedded localisation zones [Pietruszczak and Mróz, 1981, Belytschko et al., 1988]. Meshless methods have also been shown to be capable of providing certain regularisation effects. One of the first works devoted to the investigation of the regularisation properties of meshless methods is a paper by Chen et al. [Chen et al., 2000], where the authors, focusing on *moving least square* and *reproducing kernel* approximations, pointed out that these methods posses an *intrinsic nonlocality* due to the presence of weight functions whose support size is greater than the nodal spacing. They also emphasised that a further regularisation effect can be introduced when an assumed strain method based on the direct discretization of a nonlocal equivalent strain measure is adopted. Recently, in a paper by Wang and Li [Wang and Li, 2012], also the SCNI technique [Chen et al., 2001] have been shown to be able to provide regularisation effects in localisation problems.

SPIM strategies present some analogies with the aformentioned methods and are also capable to provide regularisation effects, as pointed out by Gori et al. [Gori et al., 2019b]. Despite the absence of weight functions (which are present in MLS approximations), also PIM and the RPIM approximations embed a certain nonlocality, due to the use of support domains with a size larger than the nodal spacing. As discussed by Chen et al. [Chen et al., 2000], the MLS approximation functions are capable to introduce a length scale which can be considered an *intrinsic* length, "since it resides in the approximation but is independent of the degree of discretization refinement" (Chen et al. [Chen et al., 2000], p. 1320). This independence on the discretisation is due to the use *influence domains* which allows to obtain support domains which size is independent on the nodal spacing. As it will be pointed out in Section 5.2, PIM strategies based on T-schemes for the support nodes selection can't be rigorously considered as *intrinsically* nonlocal, since the size of the support domains, though larger than the nodal spacing for certain selection schemes, depends on the refinement of the discretisation. However, a stronger nonlocal character, like the one of MLS shape functions, can be recovered by combining SPIM strategies with the influence domain technique for the selection of support nodes (Section 5.2). Another analogy with the discussion of Chen et al. [Chen et al., 2000] is the presence of the smoothing operation in SPIM strategies that, in the NS-PIM coincides with the nodal integration scheme adopted by Chen et al. [Chen et al., 2001] and by Wang and Li [Wang and Li, 2012].

5 Numerical results

5.1 Mesh objectivity

The purpose of this section is to illustrate the mesh objectivity properties induced by the intrinsic nonlocality of the SPIM approach. As it will be pointed out, SPIM strategies are capable to provide better results with respect to the standard FEM regarding mesh objectivity issues in simulations with damage models. This quality of the SPIM strategies is illustrated through the simulation performed by Gori et al. [2019b] of the plain concrete L-shaped panel depicted in Figure 10, investigated experimentally and numerically by Winkler et al. [2004]. While in each plot the experimental results obtained by Winkler et al. [2004] have also been represented, it's important to emphasise that the aim of this section wasn't to exactly reproduce the experimental results, but to illustate the capability of the adopted strategies to reproduce the general behaviour of the experimental test due to their regularisation properties. A more detailed comparison with the experimental results would have required accurate calibrations of the damage laws and, possibly, the use of damage models more complex than a simple scalar one, able to better capture the physical behaviour of the sample.

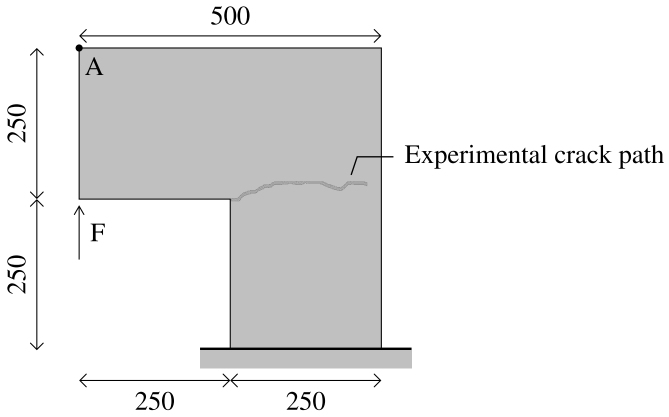

Figure 10: L-shaped panel by Winkler et al. [2004] - Geometry (measures in mm)

The concrete investigated by Winkler et al. [2004] was characterised by a Young's modulus E = 25850 N/mm^2, a Poisson's ratio ν = 0.18, tensile and compressive uniaxial strengths f$_t$ = 2.7 N/mm^2 and 4.0 N/mm^2, a fracture energy G$_c$ = 0.065 N/mm^2, and a characteristic length of the material h = 28 mm; in the following simulations its behaviour was reproduced adopting the *Mazars* scalar damage model (Equation 59), with the following parameters for the exponential damage law, α = 0.950, β = 1100 and K$_0$ = 1.12 $\times 10^{-4}$.

5.1.1 FEM simulations

The sample of Figure 10 was first investigated with the FEM, using four different discretisations (Figure 11), each one composed by three-node triangular elements in a plane-stress state, with a thickness of 100 mm. The four meshes were characterised by a different mean nodal spacing near the concave corner, equal to 25 mm, 15 mm, 10 mm, and 5 mm, while it was equal to 50 mm elsewhere. The analyses were performed adopting a loading process driven by the *generalized displacement control method* [Yang and Shieh, 1990], assuming a reference load F = 7000 N, an initial loading factor increment of 0.005, and a tollerance for convergence in relative displacement of 1 $\times$ 10^{-4}. The simulations discussed in this section were performed considering the tangent approximation of the constitutive operator, except for some of the meshfree simulations with influence domains discussed later which, due to convergence issues, required a secant approximation.

The results of the FEM analyses are illustrated in Figure 12, where the values of the vertical displacement at the point A of Figure 10 are plotted against the load factor, together with the experimental results presented by Winkler et al. [2004]. As it can be observed, the results obtained with the coarsest mesh were in good agreement with the experimental results, both in terms of peak value of the load factor and shape of the softening branch, except for an initial stiffness higher than the one observed in the experiment; this issue however, is common to other simulations

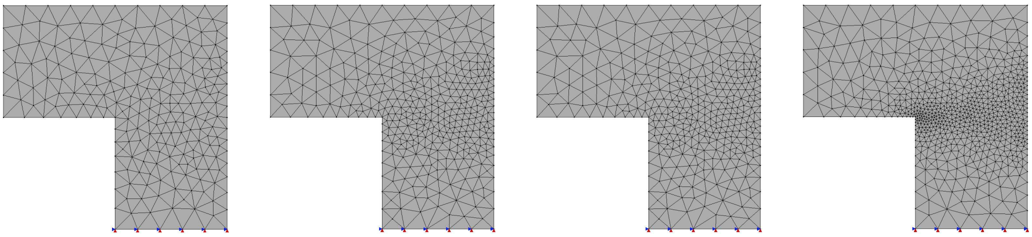
(a) Mesh 1 (b) Mesh 2 (c) Mesh 3 (d) Mesh 4

Figure 11: L-shaped panel - FEM meshes

of such a test that can be found in the literature, and it can be observed also in the simulations performed by Winkler et al. [2004]. However, the problem appeared to be strongly dependent on the discretisation, since the analyses performed with the other meshes showed sensibly lower peak values of the load factor. The presence of mesh dependency is also pointed out by the contour plots of the scalar damage variable illustrated in Figure 13. Indeed, despite their shape was compatible with the experimental cracking path depicted in Figure 10, the most refined meshes exhibited a narrower width.

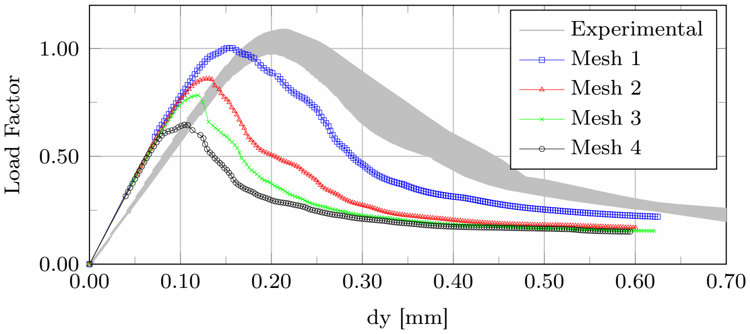

Figure 12: L-shaped panel - FEM - Equilibrium paths

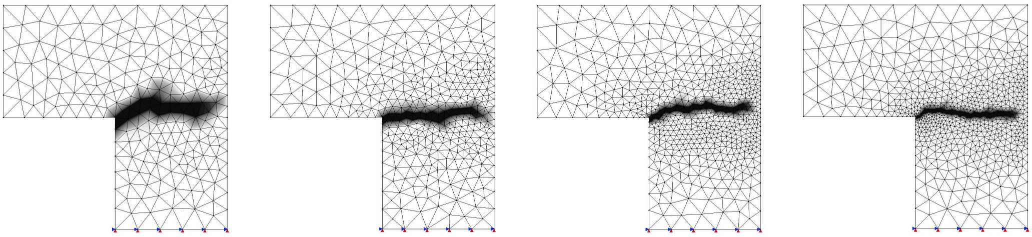
(a) Mesh 1 (b) Mesh 2 (c) Mesh 3 (d) Mesh 4

Figure 13: L-shaped panel - FEM - Damaged configurations

5.1.2 SPIM simulations

Node- and edge-based discretisations were constructed according to the same procedure discussed in Section 3.2.2, i.e. using the triangular finite elements illustrated in Figure 11 as background cells, resulting in the meshes depicted in Figures 14 and 15, maintaining the same nodal distributions adopted in the FEM simulations.

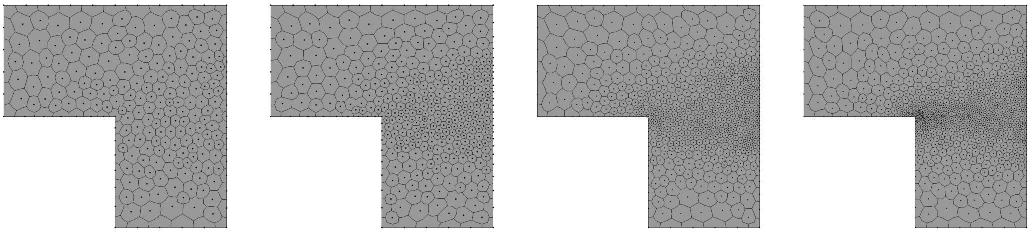

(a) Mesh 1 (b) Mesh 2 (c) Mesh 3 (d) Mesh 4

Figure 14: L-shaped panel - NS-RPIM meshes

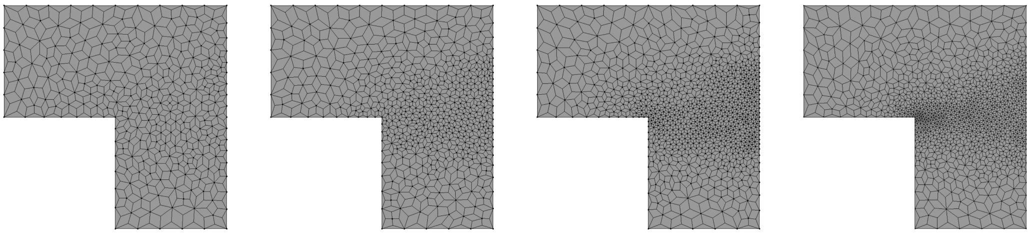

(a) Mesh 1 (b) Mesh 2 (c) Mesh 3 (d) Mesh 4

Figure 15: L-shaped panel - ES-RPIM meshes

At each integration point, the support domains were generated using both the T3 and the T6/3 schemes, while the shape functions were constructed with the radial point interpolation method with polynomial reproduction, using the exponential radial function with c = 0.002, and adopting 3 polynomial terms. The analyses were performed adopting the same loading process of the FEM simulations. The results of the analyses performed with the NS-RPIM in terms of equilibrium paths are illustrated in Figure 16, while the contour plots of the damaged configurations are depicted in Figures 17 and 18. As it can be observed, due to the upper bound approximation [Liu and Zhang, 2007], the NS-RPIM produced solutions with peak values higher than the ones obtained with the FEM. However, they exhibited the same mesh dependency issues of the finite element solutions. It is interesting to note that both the T3 and the T6/3 schemes produced almost the same results, both in terms of equilibrium paths and damage distributions.

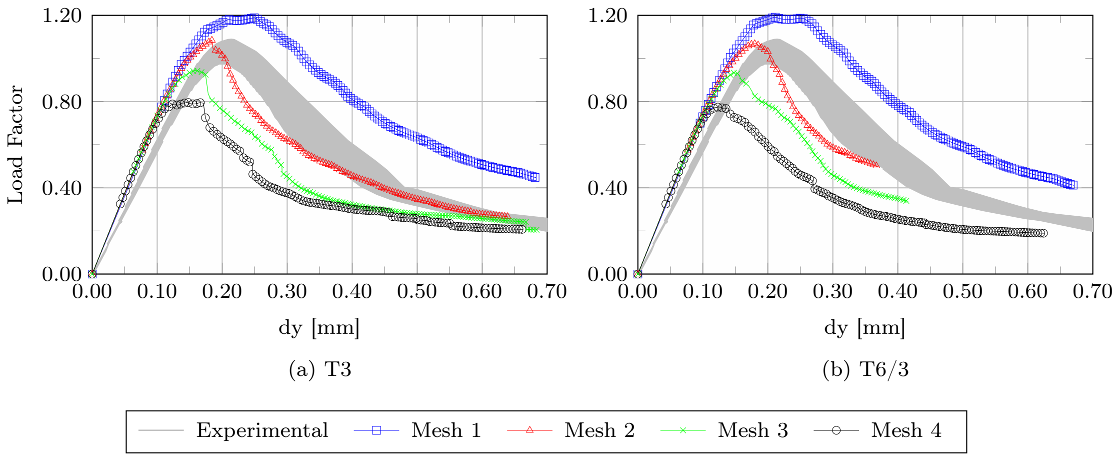

(a) T3 (b) T6/3

Figure 16: L-shaped panel - NS-RPIM - Equilibrium paths

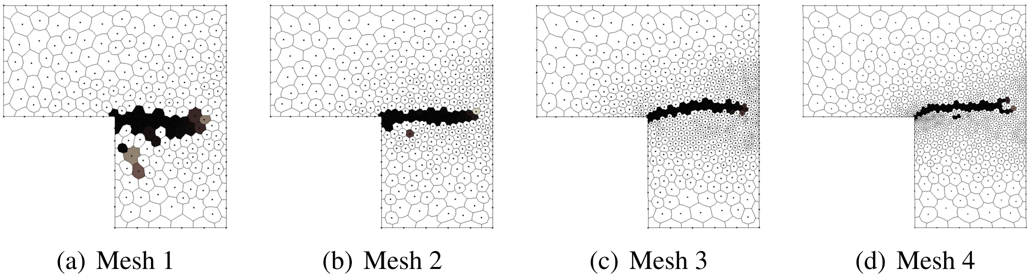
(a) Mesh 1 (b) Mesh 2 (c) Mesh 3 (d) Mesh 4

Figure 17: L-shaped panel - NS-RPIM T3 - Damaged configurations

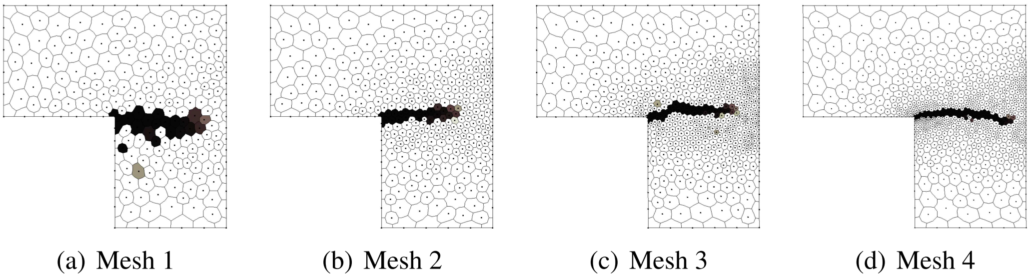
(a) Mesh 1 (b) Mesh 2 (c) Mesh 3 (d) Mesh 4

Figure 18: L-shaped panel - NS-RPIM T6/3 - Damaged configurations

As expected from the known properties of the edge-based scheme [Liu, 2009], the equilibrium paths obtained with the ES-RPIM (Figure 19) exhibited values that were intermediate between the ones of the FEM and the ones of the NS-RPIM. Regarding the equilibrium paths obtained with the T6/3 scheme it is interesting to note that while they still presented different peak values depending on the discretisation, they were characterised by less dispersed results with respect to the ones obtained with the T3 scheme. The effect of the T6/3 scheme was more evident in the meshes 2, 3, and 4, which exhibited a considerable growth of the peak values; the coarsest mesh instead, manifested almost the same peak values with the two schemes, though the post-peak branch presented a reduced decay with the T6/3 approach. The fact that the results obtained with the T6/3 scheme were less dispersed is also emphasised by the contour plots of the scalar damage variable depicted in Figures 20 and 21. While the damaged zones obtained with the T3 scheme Figure 20 presented a considerably narrower width as the discretisation was refined, the ones obtained with the T6/3 scheme appeared to be more uniform.

5.2 SPIM with influence domains

The improved results, in terms of mesh objectivity, obtained with the T6/3 scheme with respect to the T3 scheme in the ES-RPIM simulations seems to corroborate again the hypothesis that this class of methods, like other meshfree methods, are characterised by a certain degree of nonlocality embedded in their formulation, as commented in Section 4. As discussed by Gori et al. [2019b], this nonlocality can be further exploited using a different approach for the support nodes selection, switching from the T-schemes strategy to the *influence domains strategy* commonly adopted in the Element-Free Galerkin method and other meshfree methods. As discussed in Section 4, when T-schemes are being used a method can't be rigorously considered as *intrinsically* nonlocal in the sense given by Chen et al. [2000], since the spatial size of the support domain, and hence the induced internal length, depends on the discretisation. On the contrary, if the support nodes are selected using the influence domains strategy, it is possible to obtain support domains with a spatial size that is independent on the discretisation refinement. The SPIM strategy with

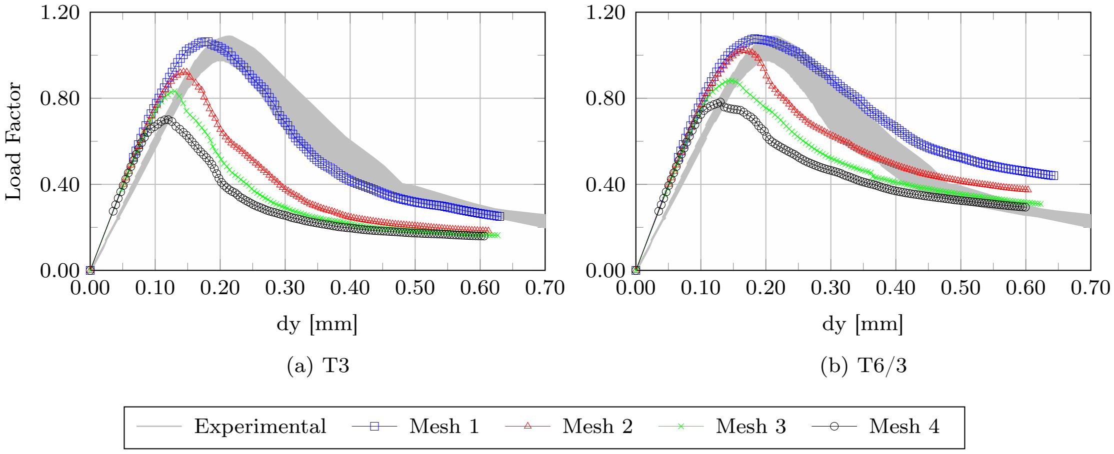

(a) T3

(b) T6/3

Figure 19: L-shaped panel - ES-RPIM - Equilibrium paths

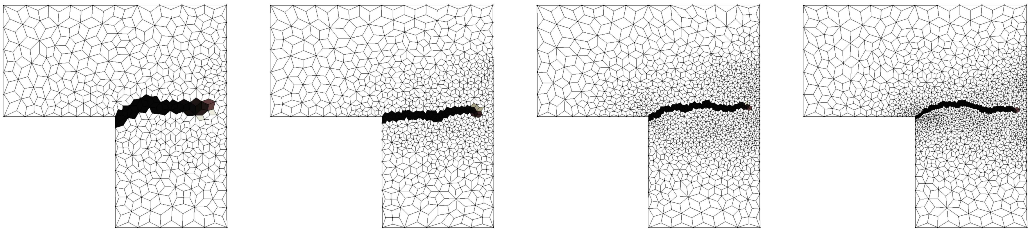

(a) Mesh 1 (b) Mesh 2 (c) Mesh 3 (d) Mesh 4

Figure 20: L-shaped panel - ES-RPIM T3 - Damaged configurations

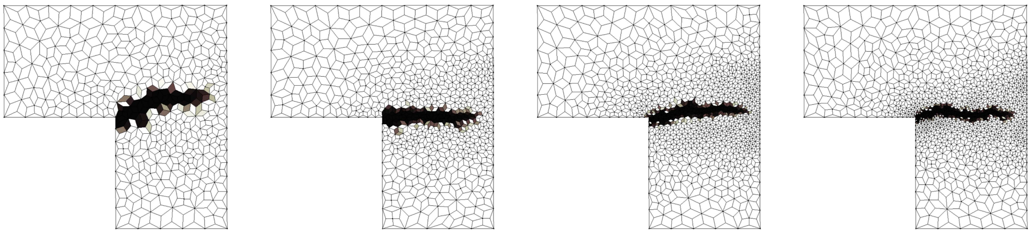

(a) Mesh 1 (b) Mesh 2 (c) Mesh 3 (d) Mesh 4

Figure 21: L-shaped panel - ES-RPIM T6/3 - Damaged configurations

influence domains presented in this section is similar to the *two-level regularisation method* proposed by Chen et al. [2000]. In the cited paper the authors showed the regularisation effects of RK discretisations in damage problems, while in case of elasto-plastic problems with more pronounced softening they adopted the aforementioned two-level regularisation, consisting in the use of a smoothing operation for the strain measure and an assumed strain method for the weak form. Despite some similarities in the approach, the strategy presented in this section differs from the one of the mentioned paper regarding the kind of shape functions, weak form and integration strategy.

The L-shaped panel was then further investigated assuming a different approach for the support nodes selection: in the zone near the concave corner (the hatched area in Figure 22), the support domains were constructed using the *influence domains strategy*, while in the other parts of the problem domain the T3 scheme was maintained. The adopted influence domains were circular, and the analyses were performed with three different values for their radius, 20 mm, 25 mm, and 30 mm. This approach was applied only to the meshes 2, 3, and 4, while for the mesh 1 the results obtained with the T3 scheme were maintained. As already stated, the idea of this approach was to try to improve the nonlocality of the SPIM strategy by using support domains larger than the ones obtainable with the sole T6/3 scheme.

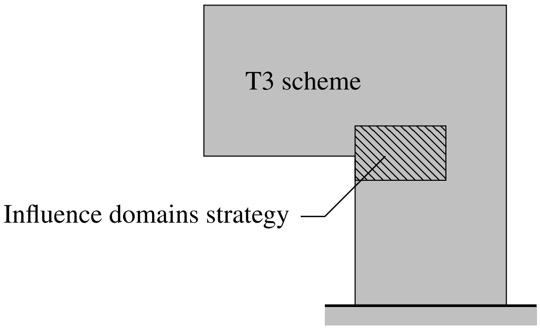

Figure 22: L-shaped panel - Area with support nodes selection via influence domains

As it can be observed in Figure 23, when circular influence domains with radius R = 20 mm were adopted, the meshes 3 and 4 exhibited almost the same equilibrium path, with a slight discrepancy in the softening branch. For the values R = 25 mm and R = 30 mm the two discretisations still manifested the same peak value, though with larger differences in the post-peak branch. Furthermore, it should be noted that to higher radii corresponded higher peak values. Considering the results obtained for the mesh 2, it is interesting to observe that as the radius of the influence domains was increased, the difference in terms of peak-values between the mesh 2 and the meshes 3 and 4 tended to decrease, emphasising the behaviour obtained with the T6/3 scheme and observed in Figure 19.

On the other hand, despite a better agreement on the value of the peak load factor, the softening branches still presented different paths. This behaviour can be ascribed, at least partially, to the fact that, as pointed out by Figure 22, the influence domains stategy was applied only near the damage initiation zone. In the other zones interested by damage propagation, that have an influence on the shape of the post-peak branch, the approximation was constructed using the T3 scheme, without the introduction of further nonlocal effects. This fact seems to be confirmed also by the contour plots illustrated in Figures 24, 25 and 26. Indeed, as it can be observed, as long as the damage developed in the area subjected to nodes selection by influence domains, the width of the damaged zones was almost the same among the three discretisations. As it started to grow outside of that area, the damaged zones became mesh dependent again.

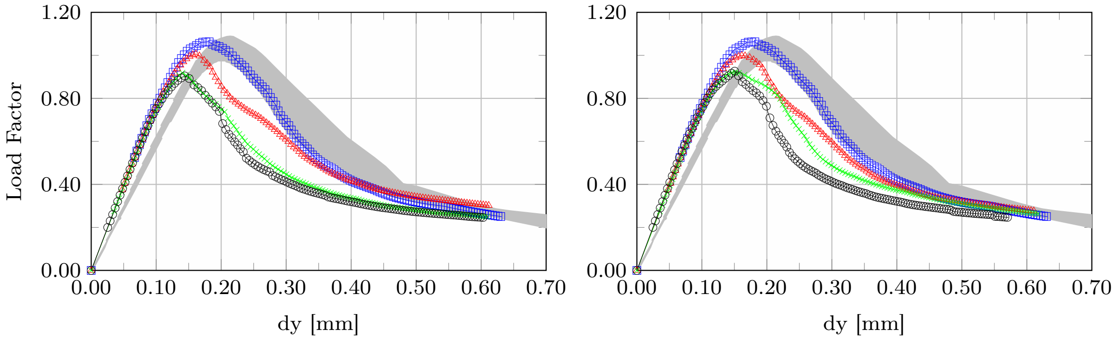

(a) R = 20 mm

(b) R = 25 mm

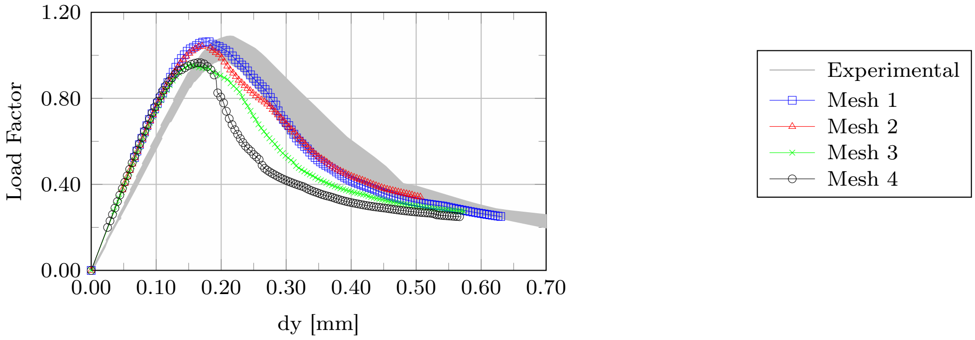

(c) R = 30 mm

Figure 23: L-shaped panel - ES-RPIM with influence domains strategy - Equilibrium paths

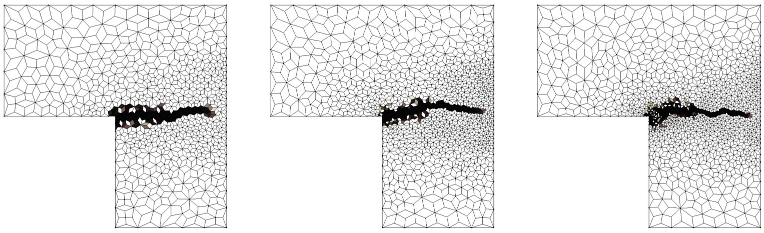

(a) Mesh 2 (b) Mesh 3 (c) Mesh 4

Figure 24: L-shaped panel - ES-RPIM with influence domains strategy - R = 20 mm - Damaged configurations

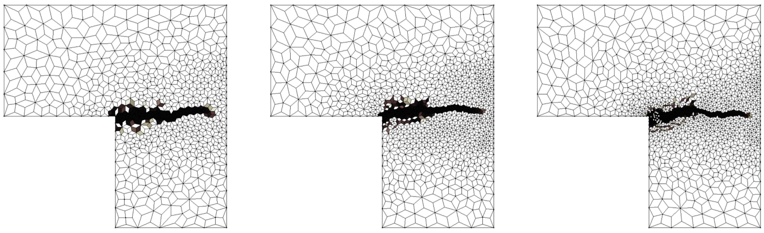

(a) Mesh 2 (b) Mesh 3 (c) Mesh 4

Figure 25: L-shaped panel - ES-RPIM with influence domains strategy - R = 25 mm - Damaged configurations

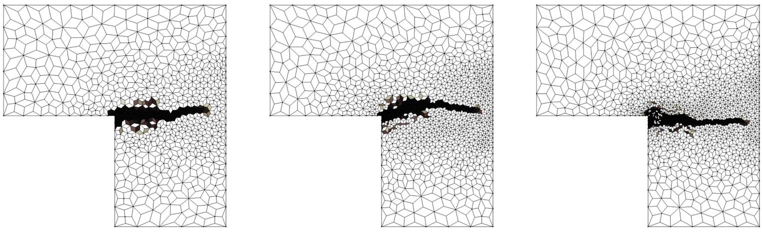

(a) Mesh 2 (b) Mesh 3 (c) Mesh 4

Figure 26: L-shaped panel - ES-RPIM with influence domains strategy - R = 30 mm - Damaged configurations

5.2.1 Drawbacks of the influence domains strategy

While the application of the influence domains strategy to PIM and RPIM shape functions exhibited certain beneficial effects concerning mesh objectivity, it also presents three main drawbacks. The first one is related to the efficiency of the numerical method. The influence domains strategy indeed, tends to generate support domains with a larger number of nodes with respect to the T-schemes, affecting the *sparseness* of the stiffness matrix of the discrete model, increasing the computational cost for the solution of the model. The effects of this issue however, may be reduced by limiting the application of such strategy to specific parts of the problem domain, as done in Figure 22 where it was applied in the area interested by damage propagation.

The second issue is related to the convergence of the iterative process for the solution of the nonlinear problem. As discussed before, while most of the simulations were performed considering the tangent approximation of the constitutive operator, the most refined mesh combined with the influence domains strategy required a *secant* approximation of the constitutive operator, in order to attain convergence. The application of the influence domains strategy to the most refined mesh resulted in support domains with a considerable number of nodes, which led to a bad conditioning of the moment matrix used for the generation of the shape functions, and then to a bad conditioning of the stiffness matrix with respect to the other situations, as illustrated in Table 1, affecting the stability of the iterative process. It is necessary to emphasise that the analysis of the most refined mesh with the influence domains strategy also required an adjustment of the shape parameter of the radial function which was modified to 0.003, since the initial value of 0.002 led to a singular stiffness matrix.

Mesh	T3	T6/3	R = 20 mm	R = 25 mm	R = 30 mm
2	1.7310×10^4	4.1281×10^4	3.1798×10^4	2.7123×10^4	3.3014×10^4
3	2.2411×10^4	6.7891×10^4	6.0680×10^4	6.2369×10^4	8.2492×10^4
4	2.5352×10^4	1.1324×10^5	4.5255×10^{16}	1.6335×10^{13}	2.3189×10^{13}

Table 1: Condition number of the initial stiffness matrix

The third and final issue is the possibility to obtain a singular moment matrix for the integration points near the domain boundary. As discussed by Liu [2009], PIM shape function suffer from singularity issues in presence of peculiar support nodes alignments, like the one that may arise when a large number of support nodes is selected on a straight domain boundary; the same issue may appear also with RPIM and RPIMp shape functions. While nodes alignments are naturally avoided with T-schemes, when using an influence domains strategy there is no such control over possible alignments.

These issues point out that the use of the influence domains strategy as a mean for improving the regularisation properties of the SPIM approach still need further investigations to guarantee a more general applicability.

5.3 Mixed-mode fracture in concrete

The previous section pointed out the mesh objectivity properties induced by the intrinsic nonlocality of the SPIM approach. In a number of situations however, such properties are not sufficient to completely regularise a simulation and further tools are needed. The purpose of the present section is then to show that the SPIM approach can be combined with other regularisation strategies, in this case the micropolar continuum theory, to provide a stronger regularisation effect. This quality of the SPIM is illustrated with the simulation performed by Gori [2018] and Gori et al. [2019a] of the four-point shear test of the plain concrete beam depicted in Figure 27, investigated experimentally by Arrea and Ingraffea [1982]; this test has been widely used in the literature as a benchmark for numerical investigations on concrete behaviour. The beam is characterised by a mixed-mode loading, with an high shear gradient between the fixed constraint and the applied load P. The failure corresponds to a curved crack path, going from the top of the notch to the point of application of the load P. Due to its characteristics, the simulation of such test is difficult with scalar-isotropic damage models, and usually requires more complex approaches, like discrete cracking methods (see, e.g. Oliver et al. [2002], Rabczuk and Belytschko [2004], de Borst et al. [2004] and Fang et al. [2008]), or special treatments for scalar damage models like the non-local approach (see, e.g. Jirásek [2007]), for example. As it will be shown in the present section, analyses performed with classic scalar damage models were not able to reproduce the experimental results of the four-point shear test, due to instabilities in the loading branch of the equilibrium paths. On the other hand, it was possible to reproduce the behaviour of the experimental test by providing the SPIM approach with a further level of regularisation, using the micropolar approach (Section 4). This result was expected for this peculiar loading condition since, in presence of high values of shear stresses, couple-stresses usually arise, leading to the activation of the internal bending length, and to the regularisation effects of the micropolar formulation.

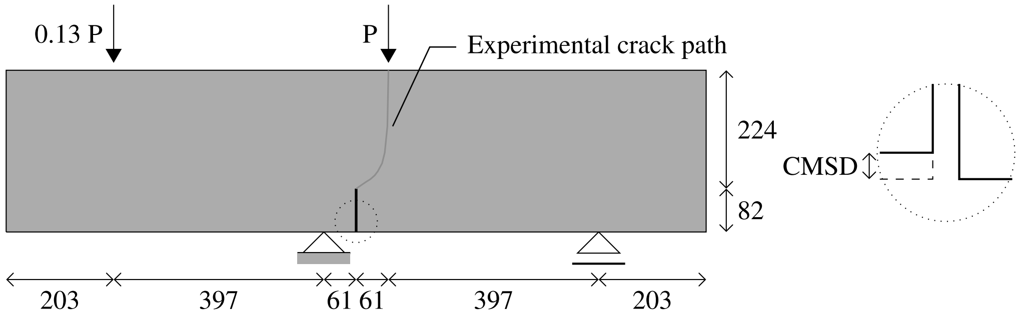

Figure 27: Four-point shear test by Arrea and Ingraffea [1982] - Geometry (measures in mm)

The concrete used by Arrea and Ingraffea [1982] in the experimental test was characterised by a Young's modulus E = 24800 N/mm^2, Poisson's ratio ν = 0.20, tensile uniaxial strength between 2.8 N/mm^2 and 4.0 N/mm^2, and fracture enegy between 0.10 N/mm^2 and 0.14 N/mm^2; these characteristics were reproduced in these simulations adopting the *Mazars* scalar damage model (Equation 59), with the following parameters for the exponential damage law (Equation 58), α = 0.950, β = 1000 and $K_0 = 1.6 \times 10^{-4}$.

5.3.1 FEM simulations

The analyses with the finite element method were performed considering meshes composed by three-node triangular elements in a plane-stress state, with a thickness of 156 mm. Three discretisations were adopted (Figure 28), with mean nodal spacing of 30 mm, 20 mm, and 10 mm between the notch and the point of application of the load P, and 70 mm elsewhere. The notch was represented as sharp, with an initial opening of 5 mm.

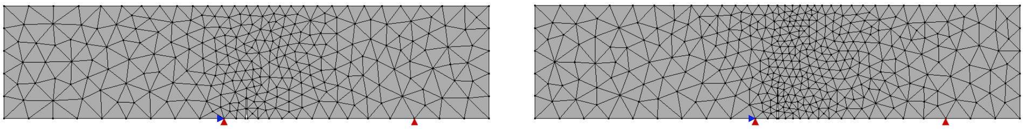

(a) Mesh 1 (b) Mesh 2

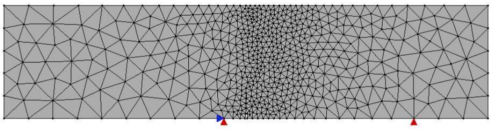

(c) Mesh 3

Figure 28: Four-point shear test - FEM meshes

The FEM analyses were performed adopting a loading process driven by a *cylindrical arc length* control method, assuming a reference load P = 130000 N, an initial loading factor increment of 0.0125, and a tollerance for convergence in relative displacement of 1×10^{-4}. All the simulations presented in this section were performed considering the tangent approximation of the constitutive operator. The results of the analyses performed with the classic medium, in terms of *crack mouth sliding displacement* (CMSD) plotted against the load factor are illustrated in Figure 29, together with the experimental results obtained by Arrea and Ingraffea [1982]. As it can be observed, no one of the three meshes was able to describe the behaviour of the beam; the meshes 1 and 2 exhibited an elastic unloading once the peak value of the load factor was reached, while the third mesh lost convergence before the maximum load factor value.

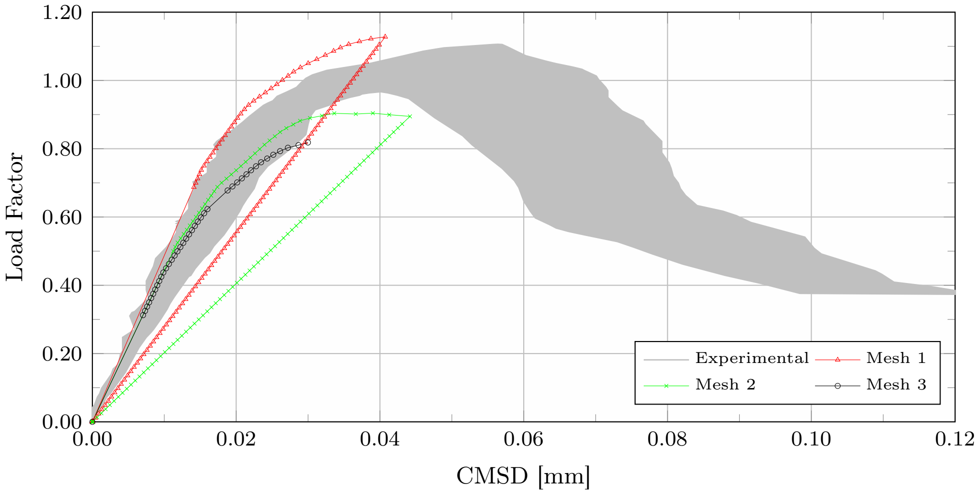

Figure 29: Four-point shear test - FEM - Equilibrium paths

The analysis of the four-point shear test was repeated for the three discretisations using the micropolar medium, with six different combinations of the additional material parameters, adopting the values 500 N/mm^2, 2500 N/mm^2, and 3500 N/mm^2 for the Cosserat's shear modulus G_c, and the values 5.0 mm and 10.0 mm for the internal bending length L_b. The results are collected in the plots of Figure 30. As it can be observed, the use of the micropolar medium with a simple scalar damage model allowed to investigate also the post-peak branch of the equilibrium paths, which were affected by both the additional material parameters; specifically, to higher values of G_c and L_b corresponded higher peak values of the load factor. Despite the fact that, on the contrary of the classic medium, the micropolar one allowed to reproduce the softening phase of the loading process, it can be observed that the solutions depicted in Figure 30 strongly depended on the discretisation, with lower peak values obtained with the most refined meshes. This fact is emphasised also by the damaged configurations illustrated in Figure 31. The damaged zones obtained with the three meshes were compatible with the expected cracking path (Figure 27); however, it can be observed that to a finer mesh corresponded a narrow damaged zone, pointing out the mesh dependency of the problem, which wasn't mitigated by the micropolar formulation.

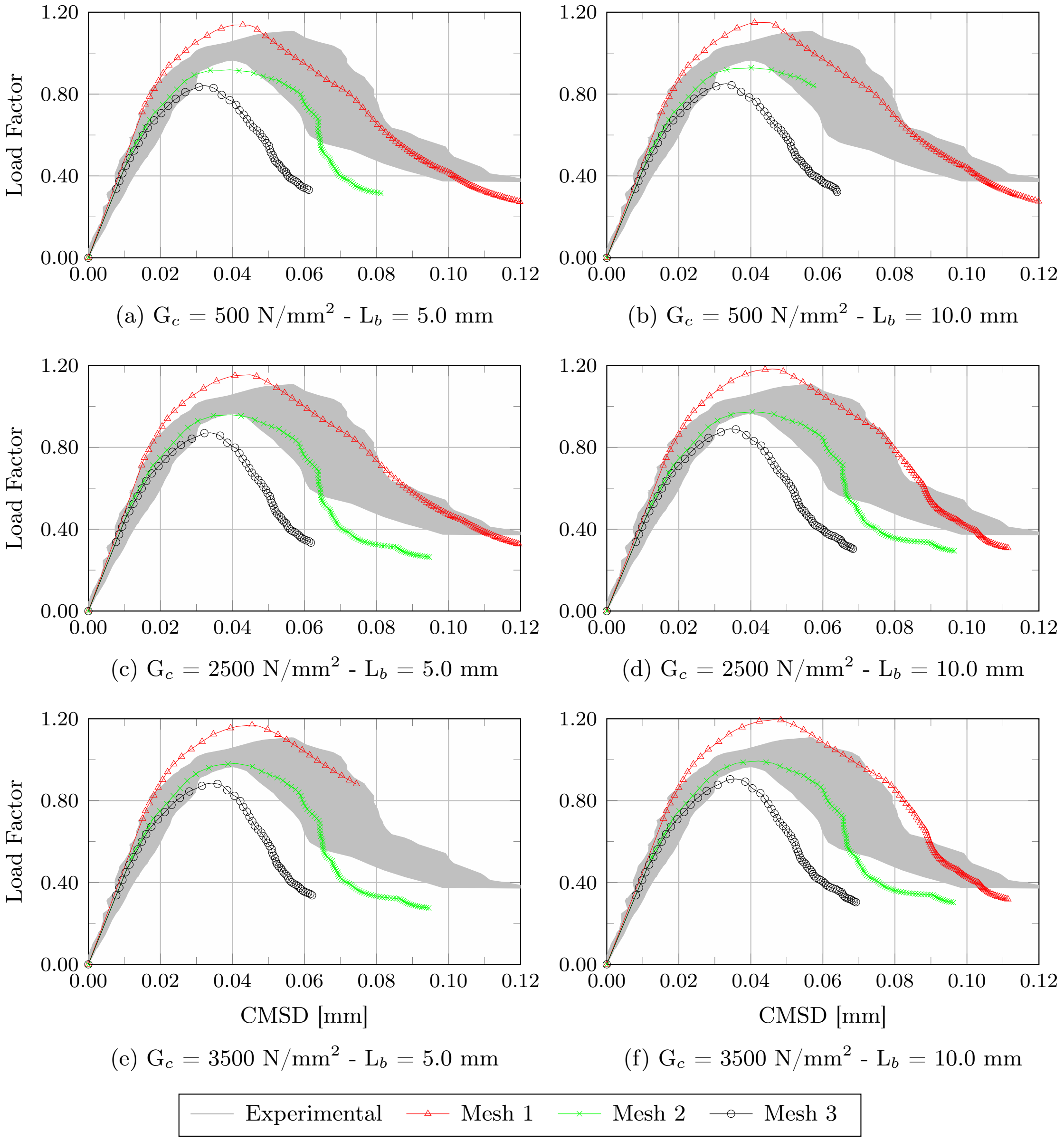

(a) $G_c = 500\ \mathrm{N/mm^2}$ - $L_b = 5.0$ mm

(b) $G_c = 500\ \mathrm{N/mm^2}$ - $L_b = 10.0$ mm

(c) $G_c = 2500\ \mathrm{N/mm^2}$ - $L_b = 5.0$ mm

(d) $G_c = 2500\ \mathrm{N/mm^2}$ - $L_b = 10.0$ mm

(e) $G_c = 3500\ \mathrm{N/mm^2}$ - $L_b = 5.0$ mm

(f) $G_c = 3500\ \mathrm{N/mm^2}$ - $L_b = 10.0$ mm

Figure 30: Four-point shear test - Micropolar FEM - Equilibrium paths

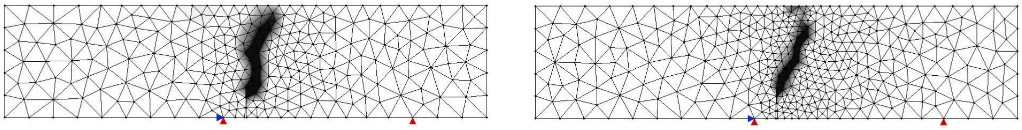

(a) Mesh 1 (b) Mesh 2

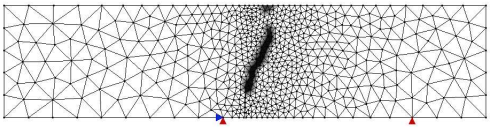

(c) Mesh 3

Figure 31: Four-point shear test - Micropolar FEM - G$_c$ = 2500 N/mm^2 - L$_b$ = 10.0 mm - Damaged configuration

5.3.2 ES-RPIM simulations

The beam of Figure 27 was investigated using also the ES-RPIM, with the discretisations depicted in Figure 32, each one obtained constructing the edge-based smoothing domains using as background cells the triangular finite elements of Figure 28, hence maintaining the same nodal distributions of the finite element meshes[17].

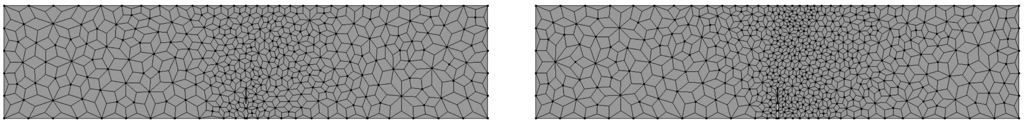

(a) Mesh 1 (b) Mesh 2

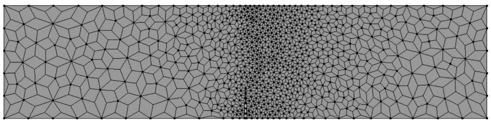

(c) Mesh 3

Figure 32: Four-point shear test - ESRPIM meshes

Regarding the generation of the support domains, both the T3 and the T6/3 schemes were adopted. The shape functions were constructed with the *radial point interpolation method with polynomial reproduction*, using the exponential radial function (15) with c = 0.002, and adopting 3 polynomial terms. As for the finite element analyses, the nonlinear simulations were performed adopting a loading process driven by a *cylindrical arc length* control method, assuming a reference load P = 130000 N, an initial loading factor increment of 0.0125, and a tollerance for convergence in relative displacement of 1×10^{-4}, considering the tangent approximation of the constitutive operator. The results of the analyses performed with the classic medium are illustrated in Figure 33. As it can be noted, in this case the behaviour of the ES-RPIM was similar to the finite element method (Figure 29); in all the simulations the models lost convergence already in the

---

[17] The simulation of the four-point shear test was performed using also node-based smoohing domains. Both polynomial and radial basis functions were tested, as well as both the selection schemes T3 and T6/3. However, neither with the classic nor with the micropolar medium it was possible to obtain satisfactory results, since damage initiated long before the expected threshold and the analyses arrested soon after the onset of damage. Hence, only the results obtained with the edge-based method are presented in this section.

loading path, except for the mesh 1 with the T3 scheme, which manifested an elastic unloading along the original loading path once the peak value was attained.

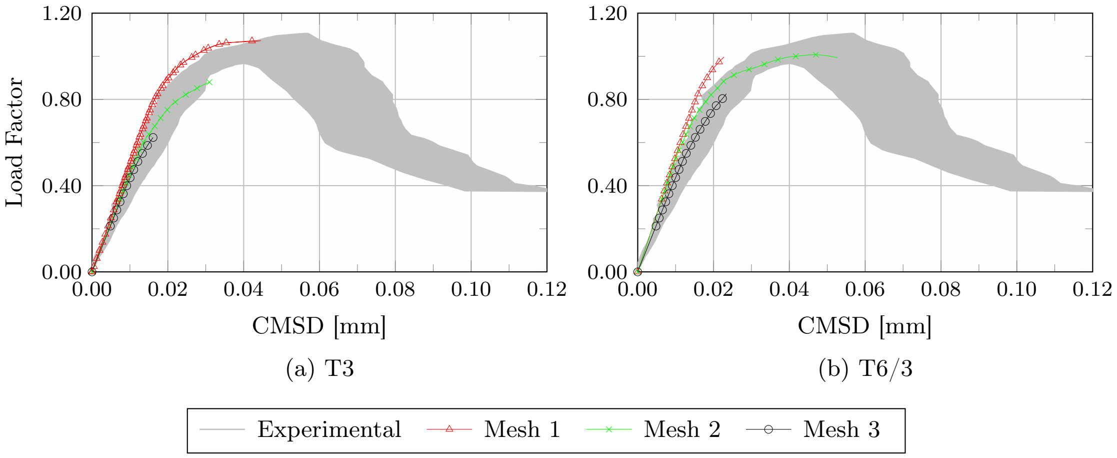

(a) T3

(b) T6/3

Figure 33: Four-point shear test - ES-RPIM - Equilibrium paths

Like in the case of the finite element method, the analyses with the micropolar medium gave significantly better results. Adopting the T3 scheme it was possible to investigate the softening phase of the loading process, except for the combinations with G_c = 500 N/mm^2, which exhibited instabilities with the meshes 1 and 3, and for the mesh 3 with the combination G_c = 2500 N/mm^2 and L_b = 10.0 mm, which also lost convegence in the loading phase, as it can be observed in Figure 34. Figure 35 illustrates the damaged configurations obtained for the three discretisations with the combination G_c = 3500 N/mm^2 and L_b = 10.0 mm, showing damaged zones compatible with the expected crack path depicted in Figure 27. However, observing the results illustrated in Figures 34 and 35 it is worth it to note that also in this case, as previously observed for the finite element method, the analyses were strongly dependent on the discretisation, with lower peak values and narrower damaged zones in the finest meshes.

The adoption of the T6/3 selection scheme in the ES-RPIM simulations led to an improvement of the results. Observing the equilibrium paths of Figure 36 it can be noted that more stable analyses were obtained, also with the combinations with G_c = 500 N/mm^2, which were characterised by instabilities in the case of the T3 scheme. Furthermore, while the simulations with the coarsest discretisation led to results well above the experimental ones, both the meshes 2 and 3 produced results that fell in the experimental rage. The most interesting result however, is that a certain mesh objectivity was observed adopting this scheme. Indeed, observing the equilibrium paths of the meshes 2 and 3 it can be noted that they exhibited similar results in terms of peak value, and were almost coincident in the final part of the softening branch, especially for the combinations with G_c = 3500 N/mm^2, with some discrepancies in the middle of the post peak branch. This result is emphasised also by the contour plots of the scalar damage variable depicted in Figure 37. Comparing Figure 37(b) with Figure 37(c) it can be observed that the two discretisations with the T6/3 scheme produced damaged zones with a similar width, while with the T3 scheme the difference in width was considerably higher (see Figures 35(b) and 35(c)).

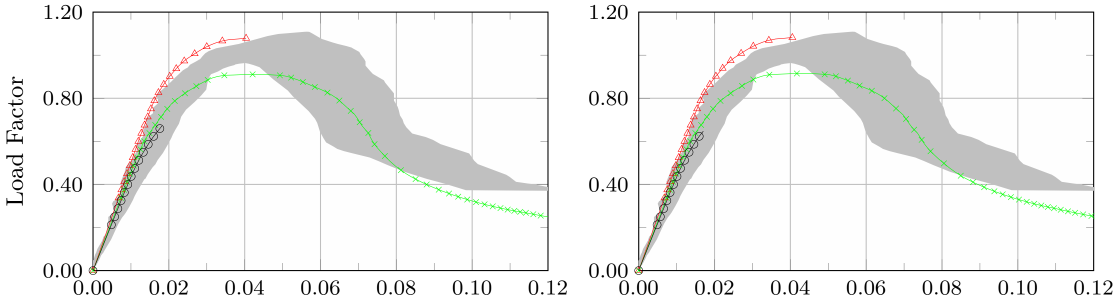

(a) $G_c = 500\ \mathrm{N/mm^2}$ - $L_b = 5.0$ mm (b) $G_c = 500\ \mathrm{N/mm^2}$ - $L_b = 10.0$ mm

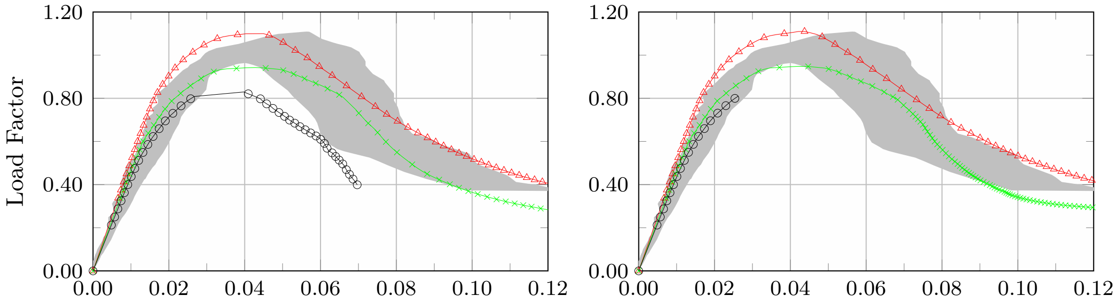

(c) $G_c = 2500\ \mathrm{N/mm^2}$ - $L_b = 5.0$ mm (d) $G_c = 2500\ \mathrm{N/mm^2}$ - $L_b = 10.0$ mm

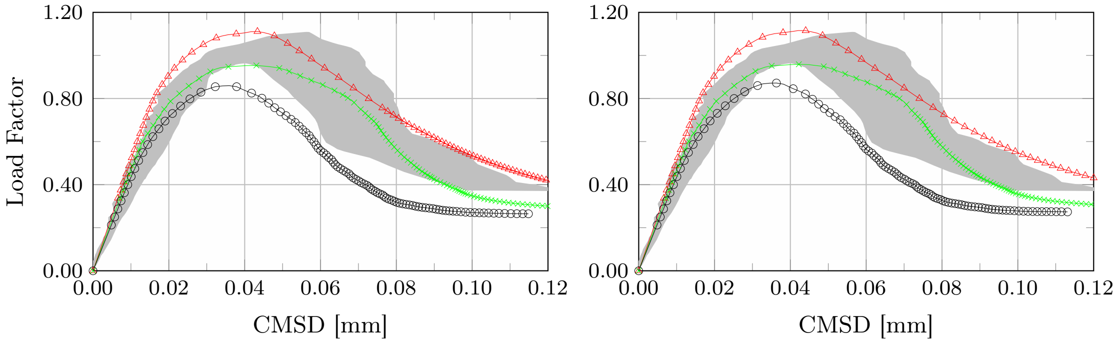

(e) $G_c = 3500\ \mathrm{N/mm^2}$ - $L_b = 5.0$ mm (f) $G_c = 3500\ \mathrm{N/mm^2}$ - $L_b = 10.0$ mm

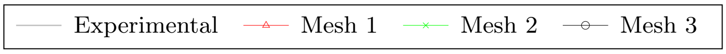

Figure 34: Four-point shear test - Micropolar ES-RPIM T3

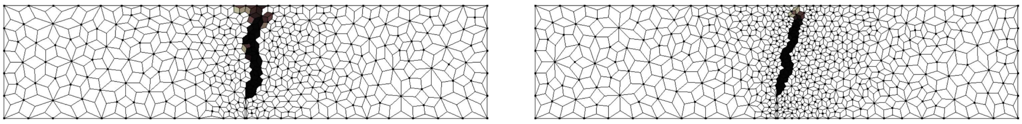

(a) Mesh 1 (b) Mesh 2

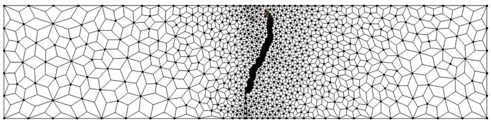

(c) Mesh 3

Figure 35: Four-point shear test - Micropolar ESRPIM-T3 - G_c = 3500 $\mathrm{N/mm^2}$ - L_b = 10.0 mm - Damaged configuration

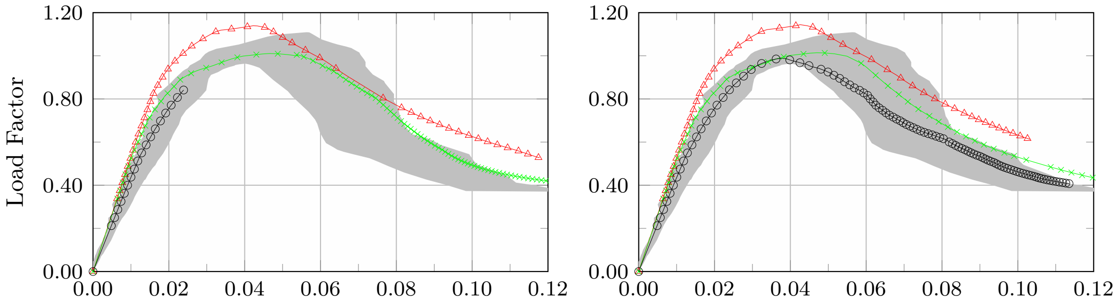

(a) $G_c = 500\ N/mm^2$ - $L_b = 5.0$ mm (b) $G_c = 500\ N/mm^2$ - $L_b = 10.0$ mm

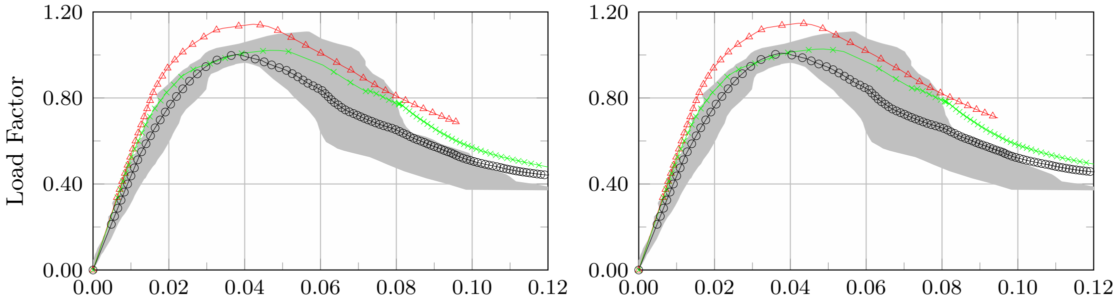

(c) $G_c = 2500\ N/mm^2$ - $L_b = 5.0$ mm (d) $G_c = 2500\ N/mm^2$ - $L_b = 10.0$ mm

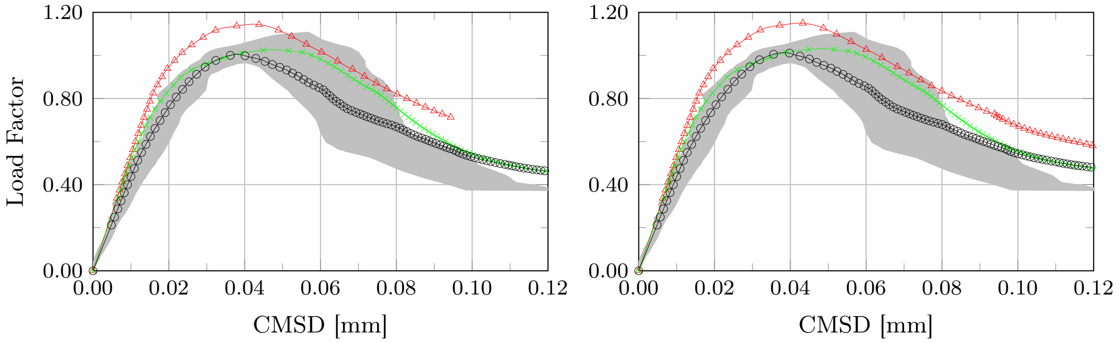

(e) $G_c = 3500\ N/mm^2$ - $L_b = 5.0$ mm (f) $G_c = 3500\ N/mm^2$ - $L_b = 10.0$ mm

Figure 36: Four-point shear test - Micropolar ESRPIM-T6/3

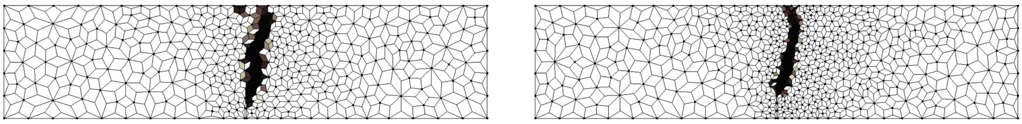

(a) Mesh 1 (b) Mesh 2

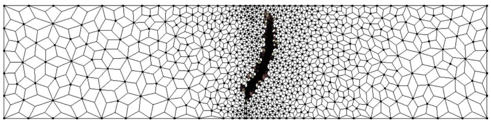

(c) Mesh 3

Figure 37: Four-point shear test - Micropolar ESRPIM-T6/3 - G_c = 3500 N/mm^2 - L_b = 10.0 mm - Damaged configuration

6 Concluding remarks

The main aim of this paper was to review the main aspects of the application of smoothed point interpolation methods, a family of meshless methods, to the problem of damage modelling. It has been clearly pointed out that this class of meshless methods is a valid alternative to deal with constitutive models that exhibit a strain-softening behaviour, such as the scalar damage model considered in the paper. Different levels of regularisation can be obtained, depending on how the meshless method is used. It has been shown that, when used as the sole regularisation strategy, SPIM techniques are not capable to provide a sufficient level of regularisation in certain situations. Whenever this occours, SPIM techniques can be combined with other regularisation strategies, like the micropolar continuum theory considered in this paper, in order to obtain a stronger regularisation effect. The paper also briefly discussed other existing results regarding regularisation effects provided by other meshless methods. Despite the promising results reviewed in this paper, further investigations seems to be necessary to truly point out the potential of meshless methods when applied to damage modelling and to other nonlinear phenomena. Among the possible studies there are:

- the evaluation of the influence of different kind of shape functions on the regularisation effects provided by SPIM strategies;
- the investigation of regularisation effects provided by other meshless methods like the MLPG, for example;
- the evaluation of the optimal size of the support domain to give a good trade-off between regularisation effects and the sparseness of the stiffness matrix;
- the association of meshless methods with other regularisation techniques.

References

M. Arrea and A. R. Ingraffea. Mixed mode crack propagation in mortar and concrete. Technical report, Departement of Structural Engineering, Cornell University, Ithaca, USA, 1982.

S. N. Atluri and T. Zhu. A new meshless Local Petrov-Galerkin (MLPG) approach in computational mechanics. *Computational Mechanics*, 22(2):117–127, 1998.

H. Badnava, M. Mashayekhi, and M. Kadkhodaei. An anisotropic gradient damage model based on microplane theory. *International Journal of Damage Mechanics*, 25(3):336–357, 2016. doi: 10.1177/1056789515586072.

G. Barenblatt. The mathematical theory of equilibrium of crack in brittle fracture. *Advances in Applied Mechanics*, 7:55–129, 1962. doi: Lastaccessed:14/04/2016.

K. J. Bathe. *Finite element procedures*. Prentice Hall, New Jersey, 1996.

Z. Bažant and F.-B. Lin. Non-local yield limit degradation. *International Journal for Numerical Methods in Engineering*, 26(8):1805–1823, 1988. doi: 10.1002/nme.1620260809.

Z. Bažant and B. Oh. Crack band for fracture of concrete. *Matériaux et Constructions*, 16:155–177, 1983.

Z. P. Bažant. Why continuum damage is nonlocal: Micromechanics arguments. *Journal of Engineering Mechanics*, 117(5):1070–1087, 1991. doi: 10.1061/(ASCE)0733-9399(1991)117:5(1070).

Z. P. Bažant and M. Jirásek. Nonlocal integral formulations of plasticity and damage: Survey of progress. *Journal of Engineering Mechanics*, 128(11):1119–1149, 2002. doi: 10.1061/(ASCE)0733-9399(2002)128:11(1119).

T. Belytschko, J. Fish, and B. Engelmann. A finite element with embedded localization zones. *Computer Methods in Applied Mechanics and Engineering*, 70:59–89, 1988.

T. Belytschko, Y. Y. Lu, and L. Gu. Element-free Galerkin methods. *International Journal for Numerical Methods in Engineering*, 37(2):229–256, 1994.

I. Carol, E. Rizzi, and K. J. Willam. A unified theory of elastic degradation and damage based on a loading surface. *International Journal of Solids and Structures*, 31(20):2836–2865, 1994.

J.-S. Chen and H. Wang. New boundary condition treatments in meshfree computation of contact problems. *Computer Methods in Applied Mechanics and Engineering*, 187:441–468, 2000. doi: 10.1016/S0045-7825(00)80004-3.

J.-S. Chen, C.-T. Wu, and T. Belytschko. Regularization of material instabilities by meshfree approximations with intrinsic length scales. *International Journal for Numerical Methods in Engineering*, 47:1303–1322, 2000.

J.-S. Chen, C.-T. Wu, S. Yoon, and Y. You. A stabilized conforming nodal integration for Galerkin mesh-free methods. *International Journal for Numerical Methods in Engineering*, 50:435–466, 2001. doi: 10.1002/nme.338.

J. S. Chen, X. Zhang, and T. Belytschko. An implicit gradient model by a reproducing kernel strain regularization in strain localization problems. *Computer Methods in Applied Mechanics and Engineering*, 193:2827–2844, 2004.

J. S. Chen, W. Hu, M. Puso, and X. Zhang. Strain smoothing for stabilization and regularization of Galerkin meshfree. In M. Griebel and M. A. Schweitzer, editors, *Meshfree Methods for Partial Differential Equations III*, volume 57, pages 57–75. Springer Berlin Heidelberg, Berlin, Germany, 2007.

R. de Borst. Simulation of strain localization: a reappraisal of the Cosserat continuum. *Engineering Computations*, 8:317–332, 1991. doi: 10.1108/eb023842.

R. de Borst and M. A. Gutiérrez. A unified framework for concrete damage and fracture models including size effects. *International Journal of Fracture*, 95(1-4):261–277, 1999.

R. de Borst and H.-B. Mühlhaus. Gradient dependent plasticity: formulation and algorithmic aspects. *International Journal for Numerical Methods in Engineering*, 35:521–539, 1992. doi: 10.1002/nme.1620350307.

R. de Borst and L. Sluys. Localization in a Cosserat continuum under static and dynamic loading conditions. *Computer Methods in Applied Mechanics and Engineering*, 90:805–827, 1991. doi: 10.1016/0045-7825(91)90185-9.

R. de Borst, L. Sluys, H.-B. Mühlhaus, and J. Pamin. Fundamental issues in finite element analyses of localization of deformation. *Engineering Computations*, 10:99–121, 1993. doi: 10.1108/eb023897.

R. de Borst, M. a. Gutiérrez, G. N. Wells, J. J. C. Remmers, and H. Askes. Cohesive-zone models, higher-order continuum theories and reliability methods for computational failure analysis. *International Journal for Numerical Methods in Engineering*, 60:289–315, 2004. doi: 10.1002/nme.963.

A. Dietsche, P. Steinmann, and K. Willam. Micropolar elastoplasticity and its role in localization. *International Journal of Plasticity*, 9:813–831, 1993.

D. Dugdale. Yielding of steel sheets containing slits. *Journal of the Mechanics and Physics of Solids*, 8:100–104, 1960. doi: 10.1016/0022-5096(60)90013-2.

A. C. Eringen and D. G. B. Edelen. On nonlocal elasticity. *International Journal of Engineering Science*, 10:233–248, 1972. doi: 10.1016/0020-7225(72)90039-0.

X.-J. Fang, F. Jin, and Q.-D. Yang. Extended finite-element analysis of fractures in concrete. *Engineering and Computational Mechanics*, 161(EM4):187–197, 2008. doi: 10.1680/eacm.2008.161.4.187.

S. Fernández-Méndez and A. Huerta. Imposing essential boundary conditions in mesh-free methods. *Computer Methods in Applied Mechanics and Engineering*, 193:1257–1275, 2004. doi: 10.1016/j.cma.2003.12.019.

M. Frémond and B. Nedjar. Damage, gradient of damage and principle of virtual power. *International Journal of Solids and Structures*, 33(8):1083–1103, 1996. doi: 10.1016/0020-7683(95)00074-7.

C. Geuzaine and J.-F. Remacle. Gmsh: a 3D finite element mesh generator with built-in pre- and post-processing facilities. *International Journal for Numerical Methods in Engineering*, 79(11):1309–1331, 2009. doi: 10.1002/nme.2579.

R. A. Gingold and J. J. Monaghan. Smoothed particle hydrodynamics: theory and applications to non-spherical stars. *Monthly Notics of the Royal Astronomical Society*, 181:375–389, 1977.

M. Golberg, C. Chen, and H. Bowman. Some recent results and proposals for the use of radial basis functions in the BEM. *Engineering Analysis with Boundary Elements*, 23:285–296, 1999. doi: 10.1016/S0955-7997(98)00087-3.

L. Gori. *Failure analysis of quasi-brittle media using the micropolar continuum theory, elastic-degrading constitutive models, and smoothed point interpolation methods*. Phd thesis, Universidade Federal de Minas Gerais (UFMG), 2018.

L. Gori, S. Penna, and R. Pitangueira. An enhanced tensorial formulation for elastic degradation in micropolar continua. *Applied Mathematical Modelling*, 41:299–315, 2017a. ISSN 0307904X. doi: 10.1016/j.apm.2016.08.025.

L. Gori, S. Penna, and R. Pitangueira. Discontinuous failure in micropolar elastic-degrading models. *International Journal of Damage Mechanics*, 27(10):1482–1515, 2017b. doi: 10.1177/1056789517731137.

L. Gori, S. S. Penna, and R. L. d. S. Pitangueira. Damage modelling with smoothed point interpolation methods. In *Proceedings of the XL Ibero-Latin American Congress on Computational Methods in Engineering*, Natal, RN, Brazil, 2019a.

L. Gori, S. Silva Penna, and R. L. da Silva Pitangueira. Smoothed point interpolation methods for the regularization of material instabilities in scalar damage models. *International Journal for Numerical Methods in Engineering*, 117(7):729–755, 2019b. doi: 10.1002/nme.5974.

L. Gori, S. Silva Penna, and R. L. da Silva Pitangueira. G-space theory and weakened-weak form for micropolar media: Application to smoothed point interpolation methods. *Engineering Analysis with Boundary Elements*, 101:318–329, 2019c. doi: 10.1016/j.enganabound.2019.01.013.

M.-M. Iordache and K. Willam. Localized failure analysis in elastoplastic Cosserat continua. *Computer Methods in Applied Mechanics and Engineering*, 151:559–586, 1998. doi: 10.1016/S0045-7825(97)00166-7.

M. Jirásek. Nonlocal damage mechanics. *Revue Européenne de Génie Civil*, 11(7-8):993–1021, 2007. doi: 10.1080/17747120.2007.9692974.

S. Li, W. Hao, and W. K. Liu. Mesh-free simulations of shear banding in large deformation. *International Journal of Solids and Structures*, 37:7185–7206, 2000. doi: 10.1016/S0020-7683(00)00195-5.

G. Liu. A generalized gradient smoothing technique and the smoothed bilinear form for Galerkin formulation of a wide class of computational methods. *International Journal of Computational Methods*, 5(2):199–236, 2008. doi: 10.1142/S0219876208001510.

G. Liu. *Meshfree Methods: Moving Beyond the Finite Element Method.* CRC Press - Taylor & Francis Group, New York, USA, 2009.

G. Liu. A G space theory and a weakened weak (W^2) form for a unified formulation of compatible and incompatible methods: Part I theory. *International Journal for Numerical Mehods in Engineering*, 81:1093–1126, 2010a. doi: 10.1002/nme.2719.

G. Liu. A G space theory and a weakened weak (W^2) form for a unified formulation of compatible and incompatible methods: Part II applications to solid mechanics problems. *International Journal for Numerical Methods in Engineering*, 81:1127–1156, 2010b. doi: 10.1002/nme.2720.

G. Liu and Y. T. Gu. A point interpolation method for two-dimensional solids. *International Journal for Numerical Methods in Engineering*, 50:937–951, 2001.

G. Liu and M. B. Liu. *Smoothed Particle Hydrodynamics - A mesh free particle method.* World Scientific, Singapore, 2003.

G. Liu and G. Zhang. Upper bound solution to elasticity problems: a unique property of the linearly conforming point interpolation method (LC-PIM). *International Journal for Numerical Mehods in Engineering*, 74:1128–1161, 2007. doi: 10.1002/nme.2204.

G. Liu and G. Zhang. A normed G space and weakened weak (W^2) formulation of a cell-based smoothed point interpolation method. *International Journal of Computational Methods*, 6(1):147–179, 2009. doi: 10.1142/S0219876209001796.

G. Liu and G. Y. Zhang. Edge-based smoothed point interpolation methods. *International Journal of Computational Methods*, 5(4):621–646, 2008. doi: 10.1142/S0219876208001662.

G. Liu and G. Y. Zhang. *Smoothed Point Interpolation Methods - G Space Theory and Weakened Weak Forms*. World Scientific, 2013.

G. Liu, G. Y. Zhang, and K. Y. Dai. A linearly conforming point interpolation method (LC-PIM) for 2D solid mechanics problems. *International Journal of Computational Methods*, 2(4):645–665, 2005. doi: 10.1142/S0219876206001132.

G. Liu, K. Y. Dai, and T. T. Nguyen. A smoothed finite element method for mechanics problems. *Computational Mechanics*, 39:859–877, 2007. doi: 10.1007/s00466-006-0075-4.

G. Liu, T. Nguyen-Thoi, H. Nguyen-Xuan, and K. Lam. A node-based smoothed finite element method (NS-FEM) for upper bound solutions to solid mechanics problems. *Computers and Structures*, 87:14–26, 2009. doi: 10.1016/j.compstruc.2008.09.003.

M. B. Liu, G. R. Liu, and Z. Zong. An overview on smoothed particle hydrodynamics. *International Journal of Computational Methods*, 5(1):135–188, 2008.

W. K. Liu, S. Jun, and Y. F. Zhang. Reproducing kernel particle methods. *International Journal for Numerical Methods in Fluids*, 20(8-9):1081–1106, 1995.

W. K. Liu, S. Hao, T. Belytschko, S. F. Li, and C. T. Chang. Multiple scale meshfree methods for damage fracture and localization. *Computational Materials Science*, 16:197–205, 1999. doi: 10.1016/S0927-0256(99)00062-2.

L. B. Lucy. A numerical approach to the testing of the fission hypothesis. *The Astronomical Journal*, 82(12):1013–1024, 1977.

J. Mazars. *Application de le Mécanique de l'endommagement au comportement non lineaire et à la rupture du béton de Structure*. PhD thesis, Université Pierre et Marie Curie - Laboratoire de Mécanique et Technologie, Paris, France, 1984. (in french).

C. Miehe, F. Welschinger, and M. Hofacker. Thermodynamically consistent phase-field models of fracture: Variational principles and multi-field FE implementations. *International Journal for Numerical Mehods in Engineering*, 83:1273–1311, 2010. doi: 10.1002/nme.2861.

C. Miehe, S. Teichtmeister, and F. Aldakheel. Phase-field modelling of ductile fracture: a variational gradient-extended plasticity-damage theory and its micromorphic regularization. *Philosophical Transactions of the Royal Society A: Mathematical, Physical and Engineering Sciences*, 374(2066), 2016. doi: 10.1098/rsta.2015.0170.

J. Monaghan. Why particle methods work. *Journal on Scientific and Statistical Computing*, 3(4): 422–433, 1982.

B. Nayroles, G. Touzot, and P. Villon. Generalizing the finite element method: Diffuse approximation and diffuse elements. *Computational Mechanics*, 10(5):307–318, 1992.

A. Needleman. Material rate dependence and mesh sensitivity in localization problems. *Computer Methods in Applied Mechanics and Engineering*, 67:69–85, 1988. doi: 10.1016/0045-7825(88) 90069-2.

J. Oliver, a. E. Huespe, M. D. G. Pulido, and E. Chaves. From continuum mechanics to fracture mechanics: The strong discontinuity approach. *Engineering Fracture Mechanics*, 69:113–136, 2002. doi: 10.1016/S0013-7944(01)00060-1.

M. Ortiz, Y. Leroy, and A. Needleman. A finite element method for localized failure analysis. *Computer Methods in Applied Mechanics and Engineering*, 61(2):189–214, 1987.

R. Peerlings, R. de Borst, W. Brekelmans, and J. de Vree. Gradient enhanced damage for quasi-brittle materials. *International Journal for Numerical Methods in Engineering*, 39:3391–3403, 1996. doi: 10.1002/(SICI)1097-0207(19961015)39:19⟨3391::AID-NME7⟩3.0.CO;2-D.

R. Peerlings, M. Geers, R. de Borst, and W. Brekelmans. A critical comparison of nonlocal and gradient-enhanced softening continua. *International Journal of Solids and Structures*, 38: 7723–7746, 2001. doi: 10.1016/S0020-7683(01)00087-7.

R. H. J. Peerlings, R. De Borst, W. A. M. Brekelmans, and M. G. D. Geers. Localisation issues in local and nonlocal continuum approaches to fracture. *European Journal of Mechanics, A/Solids*, 21:175–189, 2002. doi: 10.1016/S0997-7538(02)01211-1.

S. Pietruszczak and Z. Mróz. Finite element analysis of deformation of strain-softening materials. *International Journal for Numerical Methods in Engineering*, 17:327–334, 1981.

G. Pijaudier-Cabot and Z. Bažant. Nonlocal damage theory. *Journal of Engineering Mechanics*, 113(10):1512–1533, 1987. doi: 10.1061/(ASCE)0733-9399(1987)113:10(1512).

P. L. Pozo, A. Campos, S. Lascano, S. Oller, and A. Rodriguez-Ferran. A finite points method approach for strain localization using the gradient plasticity formulation. *Mathematical Problems in Engineering*, 2014, 2014.

A. Quarteroni and A. Valli. *Numerical Approximation of Partial Differential Equations*. Springer-Verlag Berlin Heidelberg, 1994.

T. Rabczuk and T. Belytschko. Cracking particles: a simplified meshfree method for arbitrary evolving cracks. *International Journal for Numerical Methods in Engineering*, 61:2316–2343, 2004. doi: 10.1002/nme.1151.

S. S. Saliba, L. Gori, and R. L. da Silva Pitangueira. A coupled finite element-meshfree smoothed point interpolation method for nonlinear analysis. *Engineering Analysis with Boundary Elements*, 128:1–18, 2021. doi: 10.1016/j.enganabound.2021.03.015.

R. Vignjevic, N. Djordjevic, S. Gemkow, T. De Vuyst, and J. Campbell. SPH as a nonlocal regularisation method: Solution for instabilities due to strain-softening. *Computer Methods in Applied Mechanics and Engineering*, 277:281–304, 2014. doi: 10.1016/j.cma.2014.04.010.

D. Wang and Z. Li. A two-level strain smoothing regularized meshfree approach with stabilized conforming nodal integration for elastic damage analysis. *International Journal of Damage Mechanics*, 22(3):440–459, 2012. doi: 10.1177/1056789512455938.

J. Wang and G. Liu. On the optimal shape parameters of radial basis functions used for 2-d meshless methods. *Computer Methods in Applied Mechanics and Engineering*, 191:2611–2630, 2002a. doi: 10.1016/S0045-7825(01)00419-4.

J. G. Wang and G. R. Liu. A point interpolation meshless method based on radial basis functions. *International Journal for Numerical Methods in Engineering*, 54:1623–1648, 2002b. doi: 10.1002/nme.489.

B. Winkler, G. Hofstetter, and H. Lehar. Application of a constitutive model for concrete to the analysis of a precast segmental tunnel lining. *International Journal for Numerical and Analytical Methods in Geomechanics*, 28:797–819, 2004. doi: 10.1002/nag.362.

P. Wriggers. *Nonlinear Finite Element Methods*. Springer-Verlag Berlin Heidelberg, 2008. doi: 10.1007/978-3-540-71001-1.

C.-K. C. Wu and M. Plesha. Essential boundary condition enforcement in meshless methods: Boundary flux collocation method. *International Journal for Numerical Methods in Engineering*, 53:499–514, 2002. doi: 10.1002/nme.267.

G. Xotta, S. Beizaee, and K. Willam. Bifurcation investigation of coupled damage-plasticity models for concrete materials. *Computer Methods in Applied Mechanics and Engineering*, 298:428–452, 2016.

Y.-B. Yang and M.-S. Shieh. Solution method for nonlinear problems with multiple critical points. *AIAA Journal*, 28(12):2110–2116, 1990. doi: 10.2514/3.10529.

G. Zhang, Y. Li, X. Gao, D. Hui, S. Wang, and Z. Zong. Smoothed point interpolation method for elastoplastic analysis. *International Journal of Computational Methods*, 12(4), 2015. doi: 10.1142/S0219876215400137.

G. Y. Zhang, G. R. Liu, Y. Y. Wang, H. T. Huang, Z. H. Zhong, G. Y. Li, and X. Han. A linearly conforming point interpolation method (LC-PIM) for three-dimensional elasticity problems. *International Journal for Numerical Mehods in Engineering*, 72:1524–1543, 2007. doi: 10.1002/nme.2050.

Y. Q. Zhang, G. R. Liu, and X. Han. Effect of small length scale on elastic buckling of multi-walled carbon nanotubes under radial pressure. *Physics Letters A*, 349:370–376, 2006. doi: 10.1016/j.physleta.2005.09.036.

O. C. Zienkiewicz and R. L. Taylor. *The finite element method - Volume 1*. Butterworth Heinemann, Oxford, 2000.